arXiv:2006.13233v1 [astro-ph.SR] 23 Jun 2020

The Effect of Misalignment between Rotation Axis and Magnetic Field on Circumstellar Disk

Shingo Hirano,[1] Yusuke Tsukamoto,[2] Shantanu Basu,[3] and Masahiro N. Machida[4, 3]

[1]Department of Earth and Planetary Sciences, Faculty of Sciences, Kyushu University, Fukuoka 819-0395, Japan
[2]Department of Earth and Space Science, Graduate Schools of Science and Engineering, Kagoshima University, Kagoshima 890-0065, Japan
[3]Department of Physics and Astronomy, The University of Western Ontario, London, ON N6A 3K7, Canada
[4]Department of Earth and Planetary Sciences, Faculty of Sciences, Kyushu University, Fukuoka, Fukuoka 819-0395, Japan

ABSTRACT

The formation of circumstellar disks is investigated using three-dimensional resistive magnetohydrodynamic simulations, in which the initial prestellar cloud has a misaligned rotation axis with respect to the magnetic field. We examine the effects of (i) the initial angle difference between the global magnetic field and the cloud rotation axis (θ_0) and (ii) the ratio of the thermal to gravitational energy (α_0). We study 16 models in total and calculate the cloud evolution until $\sim 5000\,\mathrm{yr}$ after protostar formation. Our simulation results indicate that an initial non-zero θ_0 (> 0) promotes the disk formation but tends to suppress the outflow driving, for models that are moderately gravitationally unstable, $\alpha_0 \lesssim 1$. In these models, a large-sized rotationally-supported disk forms and a weak outflow appears, in contrast to a smaller disk and strong outflow in the aligned case ($\theta_0 = 0$). Furthermore, we find that when the initial cloud is highly unstable with small α_0, the initial angle difference θ_0 does not significantly affect the disk formation and outflow driving.

1. INTRODUCTION

Circumstellar disks are a by-product of star formation and the hosts of planet formation. Thus, the formation and evolution of circumstellar disks should be clarified in order to understand both the star and planet formation processes. Recent ALMA observations show that circumstellar disks exist even in a very early phase of star formation: the so-called Class 0 stage (e.g., Sakai et al. 2014; Ohashi et al. 2014; Lefloch et al. 2015; Plunkett et al. 2015; Ching et al. 2016; Tokuda et al. 2016; Aso et al. 2017; Lee et al. 2017, 2018). At this stage, the typical disk size is considered to be as small as $\lesssim 10\,\mathrm{au}$ (Yen et al. 2017), although large-sized disks are sometimes observed (e.g., Hara et al. 2013; Okoda et al. 2018). Very recently, the disk structures during the later Class I and II stages of star formation were also revealed by ALMA (e.g., Aso et al. 2015; Bjerkeli et al. 2016; Pérez

et al. 2016; Alves et al. 2017). The DSHARP project showed beautiful views of disks around Class II pre-main-sequence stars, in which various morphologies of ring, gap, and spiral patterns were clearly shown (Andrews et al. 2018, and references therein). Understanding the early phase of the disk evolution (i.e., Class 0 and early Class I stages) is important to better clarify the late phase of the disk (i.e., late Class I and Class II stages).

In addition to the progress in observations, numerical simulations have greatly contributed to understanding disk formation. Specifically, since the studies reported by Allen et al. (2003) and Mellon & Li (2008), the magnetic braking (problem) has been intensively discussed in the context of disk formation (Li et al. 2014). Based on early simulations, some researchers claimed that the circumstellar disk cannot be formed in the very early phase of star formation, because the angular momentum is excessively removed from the disk-forming region by magnetic braking (the so-called magnetic braking catastrophe; Mellon & Li 2009 and Li et al. 2013).

Corresponding author: Shingo Hirano
hirano.shingo.821@m.kyushu-u.ac.jp

It turns out that non-ideal magnetohydrodynamical (MHD) effects (Ohmic dissipation, ambipolar diffusion, and Hall effect) are considerably important to investigate the disk evolution, because a nascent disk forms in a magnetically inactive region where the magnetic field is weakened by Ohmic dissipation and ambipolar diffusion (Dapp & Basu 2010; Dapp et al. 2012; Tomida et al. 2015; Masson et al. 2016; Tsukamoto et al. 2018, see also reviews by Tsukamoto 2016 and Wurster & Li 2018a). The diffusion rates of Ohmic dissipation and ambipolar diffusion strongly depend on the star-forming environment. The amount of charged particles and dust grains and the strength of cosmic rays determine the coefficients of magnetic diffusion rates and therefore the resultant disk size (Marchand et al. 2016; Zhao et al. 2016, 2018; Wurster et al. 2018b; Koga et al. 2019).

The Hall effect is also important for disk formation because it can generate toroidal magnetic fields from poloidal fields in the collapsing cloud. This strengthens or weakens the magnetic braking depending on the relative direction of the magnetic field and the rotation axis (magnetic field parallel or anti-parallel to rotation axis; e.g., Krasnopolsky et al. 2011; Tsukamoto et al. 2015b, 2017). In addition to the non-ideal MHD effects, some studies showed that turbulence in the star-forming core can play a role in the formation and evolution of circumstellar disks even when the prestellar cloud has a strong magnetic field (Santos-Lima et al. 2013; Seifried et al. 2012, 2013).

Several scenarios have been offered to explain the observed range of disk sizes and masses. The disk size in the early phase (or Class 0 stage) could vary for prestellar clouds with different initial magnetic field strengths and rotation rates (e.g., Masson et al. 2016). Fundamentally, the disk size is determined by the balance between the angular momentum falling into the central region and that transported outward by the magnetic effects (Machida et al. 2011). An initially rapid rotation can produce a large-sized disk and a strong magnetic field can suppress the disk size growth. The initial cloud shape and the distributions of gas density, angular velocity, and magnetic field would also change the disk size (see § 1 of Gray et al. 2018). Note, however, that Hennebelle et al. (2016) claimed that the disk size is determined only by the magnetic field strength of the disk and the ambipolar diffusion coefficient in their analytic study.

Most three-dimensional (3D) MHD simulations have, for simplicity, studied aligned rotators, i.e., the rotation axis of the prestellar cloud is parallel to the global magnetic field (e.g., Tomisaka 2002; Machida et al. 2004; Banerjee & Pudritz 2006; Tomida et al. 2013; Tsukamoto et al. 2015), and a comprehensive picture has emerged in this scenario (see Inutsuka 2012). For the first time, Matsumoto & Tomisaka (2004) and Matsumoto et al. (2006) investigated the misalignment effect, i.e., when the rotation axis of the initial cloud is

misaligned with the global magnetic field, with their three dimensional MHD simulations. Then, Hennebelle & Ciardi (2009) pointed out that the disk formation process is significantly affected by misalignment. Since then, many researchers have discussed the importance of misalignment in the process of disk formation (e.g., Joos et al. 2012, and see §2 for details). The classical effects of magnetic braking will tend to bring a prestellar core into alignment, since angular momentum that is perpendicular to the global magnetic field is lost more efficiently than the parallel component (Mouschovias & Paleologou 1979, 1980a). On the other hand, the presence of turbulence could produce an angle difference (i.e., misalignment) between the magnetic field and rotation vector (Joos et al. 2013; Krumholz et al. 2013; Matsumoto et al. 2017). Thus, a misalignment seems to be a natural consequence in clouds with both turbulence and magnetic field.

This study focuses on the effect of misalignment on the disk formation. Using a resistive MHD simulation with a sink cell, we investigate the evolution of star-forming cloud cores in which the rotation axis of the initial cloud is not aligned with the global magnetic field. The initial state is still not highly turbulent, and maintains other symmetries even though there is misalignment (for details, see §2). We believe that disk formation should be investigated in this still idealized setting in order to proceed in a step-by-step manner, rather than trying to investigate it a very complicated environment such as a highly turbulent cloud. Finally, we comment on the relation between our previous (Machida et al. 2020) and present studies, in which the initial conditions (or initial prestellar clouds) are almost the same. Machida et al. (2020) focused on the small scale structures only for $\sim 500\,\mathrm{yr}$ after protostar formation. They resolved a protostar without a sink cell and qualitatively compared the directions of the jet, disk and local magnetic field with those of observations. In this study, we use a sink cell and focus on the long-term ($\sim 5000\,\mathrm{yr}$) evolution of the circumstellar disk and outflow and the efficiency of disk formation.

Our paper is structured as follows. We summarize the past misalignment studies in §2. Numerical settings and initial conditions of our study are described in §3. Our simulation results are presented in §4. We discuss the misalignment and disk formation in §5, and compare simulations with observations in §6. We summarize our results in §7.

2. PAST STUDIES

We first comment on analytic studies, which had been performed mainly by Mouschovias and his collaborators (e.g., Mouschovias & Paleologou 1979, 1980a,b; Mouschovias & Morton 1985; Mouschovias & Paleologou 1986). They investigated the efficiency of magnetic braking in different configurations of the magnetic field. It should be noted that although magnetic braking from

a collapsing cloud core was considered in some such studies during 1970s and 1990s (see also Basu & Mouschovias 1994, 1995a,b), they did not specifically focus on the circumstellar disk formation.

Mouschovias & Paleologou (1980a) showed that magnetic braking is more efficient in the perpendicular configuration than in the aligned uniform configuration, because a strong magnetic tension force brakes the disk (Figure 1h). On the other hand, magnetic braking in the aligned fan-shaped configuration can be more efficient than in the perpendicular configuration (Mouschovias 1983, 1985), due to the large lever arm introduced by the fanning out of field lines. Thus, the analytic studies imply that magnetic braking can have efficiency in the following order: (1) aligned fan-shaped, (2) perpendicular, and (3) aligned uniform configuration. Note that the quantitative estimates and equations about magnetic braking are well summarized in Joos et al. (2012) and Tsukamoto et al. (2018).

Here, we define θ_0 as the angle between the rotation axis and magnetic field of the initial cloud. For simplicity, we only consider a uniform magnetic field as the initial configuration of prestellar cloud cores. In analytical studies, two angles $\theta_0 = 0°$ and $90°$ were only considered. Figure 1 displays such configurations of magnetic field. We call $\theta_0 = 0°$ the aligned case (panels a–c), and $\theta_0 = 90°$ the perpendicular case (d–h). Although we give special attention to the perpendicular case, it is also included in the misaligned case ($\theta_0 \neq 0°$). In addition, in a collapsing cloud (rather than an initial prestellar cloud), the aligned case is further classified into aligned uniform (Figure 1a) and aligned fan-shaped (Figures 1b and c) cases.

The efficiency of magnetic braking is determined by the moment of inertia of the reservoir of angular momentum. In the star formation process, a massive infalling envelope (or pseudodisk) brakes a less massive rotationally-supported disk to which it is connected through magnetic field lines. Thus, the configuration of the magnetic field significantly affects the efficiency of the magnetic braking, because the moment of inertia is determined by the volume (or mass and size) swept by the Alfvén waves. For example, even in the aligned cases, the moment of inertia for the aligned fan-shaped configuration is larger than that for the aligned uniform configuration because the fan-shaped magnetic field lines connect to the large volume of the infalling envelope that has a large lever arm and a large amount of mass (Figures 1b and c).

The efficiency of magnetic braking also depends on the magnetic field strength, gas density and pitch angle (for the perpendicular case) and opening angle (for the aligned fan-shaped case) of magnetic fields, which would change with time in the star formation process. For example, in the aligned case, the magnetic field configuration is approximately represented by the aligned uniform configuration in the very early accretion phase, while it
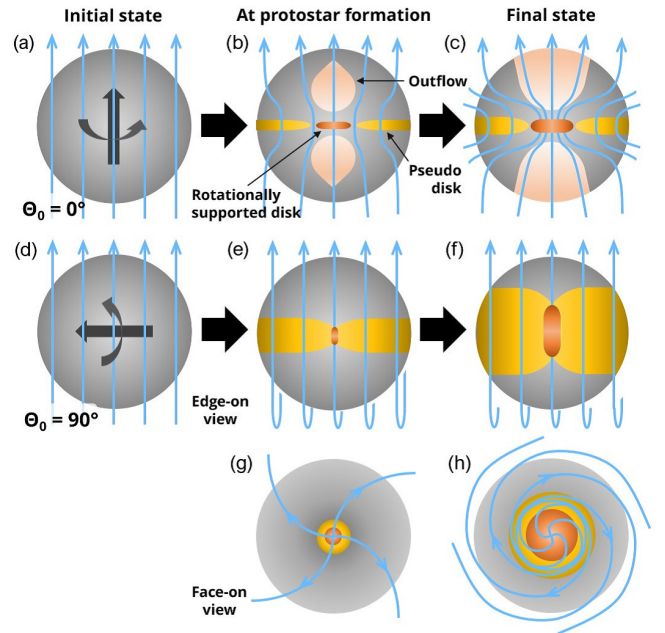

Figure 1. Schematic view of the time sequence of a star-forming cloud for the aligned ($\theta_0 = 0°$; panels a–c) and perpendicular ($\theta = 90°$; d–h) cases. Panels (a)–(f) are the edge on view, while panels (g) and (h) correspond to the face-on view of panels (e) and (f), respectively. The large black arrow indicates time evolution. Magnetic field lines are indicated by blue lines. Gray, yellow and orange regions indicate the whole star-forming cloud, pseudodisk, and rotationally-supported disk, respectively. In panels (a) and (d), the large black arrow in the sphere corresponds to the rotation axis. In panels (b) and (c), the outflow is represented by a red color.

gradually transforms to the aligned fan-shaped configuration as the protostar and disk evolve, as described in Figures 1(a)–(c). Therefore, it is very difficult using only analytic studies to clearly state which case or configuration dominates during the evolution. 3D simulations are necessary to quantitatively investigate the relation between disk formation and magnetic braking.

In Table 1, we summarize 3D MHD simulations that investigated the misalignment nature in collapsing clouds, in addition to our present study. We further comment on each study here.

The ideal MHD approximation was used in all the studies, with the exception of Masson et al. (2016), Tsukamoto et al. (2018) and Machida et al. (2020). Except for Tsukamoto et al. (2018), the barotropic equation of state (hereafter EOS) was used to mimic the thermal evolution of star-forming cloud cores, and a sink or stiff EOS was used to accelerate the time evolution in simulations since the time step shortens as the cloud collapse proceeds. Although Tsukamoto et al. (2018) calculated the cloud evolution resolving the protostar

Table 1. Summary of past studies and this study

Authors	I/N MHD	EOS	μ_0	θ_0 (°)	α_0	β_0	Sink/EOS	Disk
Matsumoto & Tomisaka (2004)	Ideal	Barotropic	2, 4, 10	0, 45, 70, 80, 90	0.5	0.02	Stiff EOS	
Hennebelle & Ciardi (2009)	Ideal	Barotropic	2, 5, 16	0, 10, 20, 60, 90	0.25	0.03	Stiff EOS	Y/N
Joos et al. (2012)	Ideal	Barotropic	2, 3, 5, 17	0, 20, 45, 70, 80, 90	0.25	0.03	Stiff EOS	Y/N
Li et al. (2013)	Ideal	Barotropic	2.9, 4.9, 9.7	0, 45, 90	0.75	0.025	Sink (7 au)	Y/N
Lewis et al. (2015)	Ideal	Barotropic	5	0, 10, 20, 45, 60, 90	0.37	0.005	Sink (1 au)	
Masson et al. (2016)	Non-Ideal	Barotropic	2, 5	0, 40	0.25	0.02	Stiff EOS	Y
Tsukamoto et al. (2018)	Non-Ideal	RMHD	4	0, 45, 90	0.2, 0.4, 0.6	0.03	N	Y
Machida et al. (2020)	Non-Ideal	Barotropic	1.2	0, 5, 10, 30, 45, 60, 80, 85, 90	0.39	0.026	Stiff EOS	Y
This study	Non-Ideal	Barotropic	3	0, 10, 30, 45, 60, 80, 90	0.2, 0.4, 0.6	0.02	Sink (0.5 au)	Y

Note— Column 1: author name(s) for each study; Column 2: whether non-ideal MHD effects are included (Non-Ideal) or not (Ideal); Column 3: whether the barotropic equation of state is used (Barotropic) or not (RMHD); Column 4: mass-to-flux ratio normalized by the critical value used; Column 5: initial angle between the rotation axis and magnetic field direction; Columns 6 and 7: ratio of the thermal (α_0) and rotational (β_0) energy relative to the gravitational energy adopted; Column 8: whether the sink (Sink) or the stiff equation of state (Stiff EOS) is used or not (N), and the sink radius is written when the sink is used; Column 9: whether the rotationally-supported disk appears (Y) or not, in which Y/N means that the disk appears only when the initial magnetic field is weak. In the table, a space means no mention about the corresponding item.

without sink particles, they could not calculate the disk evolution for a long duration.

The pioneering work of Matsumoto & Tomisaka (2004) investigated the rate of angular momentum transported by the magnetic braking with a stiff EOS. Matsumoto & Tomisaka (2004) calculated the main accretion phase for a short duration and claimed that magnetic braking is more efficient in the perpendicular case than in the aligned case. Although they did not comment on whether or not the rotationally-supported disk forms, they showed that the angular momentum in the perpendicular case is less than in the aligned case. They calculated the cloud evolution only for $\lesssim 600$ yr after the adiabatic core formation, which corresponds to the very early main accretion phase.

Using a stiff EOS, Hennebelle & Ciardi (2009) calculated the disk evolution for ~ 5000 yr after the adiabatic core formation and pointed out that the efficiency of magnetic braking decreases as the initial angle difference θ_0 increases. In addition, no disk appears when the angle is as small as $\theta_0 \simeq 0°$ even in a weakly magnetized cloud ($\mu_0 = 5$). They interpreted that the decrease of magnetic braking efficiency in the cloud with large θ_0 is attributed to the formation of thick pseudodisk. When the angle is $\theta_0 \neq 0°$, the twisted magnetic fields amplify the magnetic pressure and thicken the pseudodisk. The pseudodisk is a reservoir of the angular momentum and is rotating with a sub-Keplerian velocity. Thus, the existence of such a thick pseudodisk decreases the efficiency of the magnetic braking (see also Ciardi & Hennebelle 2010).

Using the same numerical code as in Hennebelle & Ciardi (2009), Joos et al. (2012) investigated the disk formation with various parameters of the initial cloud. They also concluded that the initial angle difference between $\boldsymbol{J}$ and $\boldsymbol{B}$ (i.e., $\theta_0 \neq 0°$) promotes the disk formation. However, unlike Hennebelle & Ciardi (2009), they claimed that a fan-like configuration of the magnetic fields, which is realized with a small θ_0, increases the efficiency of the magnetic braking. Thus, a large-sized disk tends to appear with a large θ_0.

Li et al. (2013) also showed that the disk formation is promoted with large angle difference (or large θ_0). Thus, their result is qualitatively the same as in Hennebelle & Ciardi (2009) and Joos et al. (2012). By estimating the magnetic torques, they showed that magnetic braking in the aligned case ($\theta_0 = 0°$) is more efficient than in the misaligned case ($\theta_0 \neq 0°$). In addition, they pointed out that the protostellar outflow weakens as θ_0 increases and does not appear in the perpendicular case ($\theta_0 = 90°$). Since the outflow directly removes the angular momentum from the central (or disk forming) region, it should greatly affect the formation of a rotationally-supported disk. Furthermore, they claimed that magnetic interchange instability (Li & McKee 1996; Tassis & Mouschovias 2005) possibly disrupts the disk formation. However, the sink radius adopted in Li et al. (2013) is too large to properly investigate the disk formation (Machida et al. 2014, 2016).

Lewis et al. (2015) investigated the disk formation in the misaligned cases with a small sink radius of 1 au and also showed that the outflow weakens as the angle differ-

ence (θ_0) increases. However, they did not comment on the formation of rotationally-supported disk in detail.

In these studies (Matsumoto & Tomisaka 2004; Hennebelle & Ciardi 2009; Joos et al. 2012; Li et al. 2013; Lewis et al. 2015), the effects of magnetic braking on the disk formation in both aligned and misaligned cases were investigated in the ideal MHD approximation. Then, Masson et al. (2016) investigated the evolution of both cases with their non-ideal MHD simulations, in which the magnetic field weakens in a high-density region due to ambipolar diffusion. Note that they did not include the Ohmic dissipation. Unlike previous studies, they concluded that misalignment nature does not significantly affect the disk evolution because the magnetic field dissipates in the disk forming region. However, they calculated the cloud evolution only with two angle cases ($\theta_0 = 0$ and $40°$). In addition, the disk radius is larger in the misaligned case ($\theta_0 = 40°$) than in the aligned case ($\theta_0 = 0°$) for a strongly magnetized cloud ($\mu_0 = 2$), while a large-sized disk appears in the aligned case for a weakly magnetized cloud. Thus, it is difficult to conclude the effect of misalignment only from this study.

Most recently, Tsukamoto et al. (2018) pointed out that gravitational stability of the prestellar core significantly affects the results. They concluded that the difference between Matsumoto & Tomisaka (2004) and other studies is caused by the difference in α_0 that is defined as the ratio of thermal to gravitational energy and controls the mass accretion rate (Matsushita et al. 2017). With a small α_0, the cloud is gravitationally very unstable, the mass accretion rate on the disk is high and magnetic field lines are rapidly advected inward in the collapsing cloud, allowing less magnetic braking. Therefore, in such a case, a large-sized disk tends to appear independent of the parameter θ_0. On the other hand, with a large α_0, the cloud is marginally gravitationally unstable and the slower collapse allows the magnetic field and magnetic braking to play a significant role in determining the disk size. However, Tsukamoto et al. (2018) calculated the disk formation only in the very early accretion phase, because they did not use sink particles (see also Machida et al. 2020).

To summarize, Matsumoto & Tomisaka (2004) implied that the misalignment nature *suppresses* the disk formation, while other studies claimed that it *promotes* the disk formation. The resolution to this discrepancy is that in addition to the parameter θ_0, the non-ideal MHD effects and the parameter α_0 are also significant for considering the disk formation. Nevertheless, with non-ideal MHD simulations, no one investigated a long-term evolution of a rotationally-supported disk with investigation of the parameters θ_0 and α_0. The purpose of this study is to further the study of the misalignment problem: whether the misalignment nature promotes or suppresses the disk formation. Using non-ideal MHD

simulations, we investigate the disk formation using a wide range of parameters as described in Table 1.

3. INITIAL CONDITION AND NUMERICAL SETTINGS

The initial condition and numerical settings in this study are almost the same as in our past studies (Machida et al. 2006, 2007; Machida & Hosokawa 2013). We use our nested grid code, in which the rectangular grids of $(i, j, k) = (64, 64, 64)$ are superimposed (Machida et al. 2004, 2005; Machida & Matsumoto 2012). The convergence of the numerical resolution is described in Appendix A. We use the index "l" to describe a grid level. The grid size $L(l)$ and cell width $h(l)$ of the l-th grid are twice larger than those of $(l + 1)$-th grid (e.g., $L(l) = 2L(l + 1)$ and $h(l) = 2h(l + 1)$). In the simulation, we resolve the Jeans wave length with at least 16 cells, and a new finer grid is automatically generated to ensure the Truelove condition (Truelove et al. 1998).

We solve the resistive MHD equations with the barotropic EOS (equations 1–7 of Machida & Matsumoto 2012). The diffusion rate of Ohmic resistivity is described in Machida et al. (2007) and Machida & Matsumoto (2012). The differences in numerical settings between past studies and our study are also described in Table 1.

As described in §2, the past studies pointed out the importance of the parameters θ_0 and α_0. We executed two types of simulations to examine the parameter dependence on θ_0 and α_0, respectively:

(A) simulations with different angles θ_0 (hereafter we referred to as "Simulations A")

(B) simulations with different gravitational stabilities α_0 (hereafter we referred to as "Simulations B").

We executed 16 simulations in total. Each simulation required 2–4 months of wall-clock-time. Since the simulations take a very long time to run, and were performed over the course of more than one year, all simulations were not coordinated to have exactly the same initial conditions. Therefore, Simulations A and B differ slightly even when the parameters θ_0 and α_0 are the same (for details, see below). For easy understanding, the initial conditions of Simulations A and B are separately described in the following subsections (§3.1 and 3.2).

In both Simulations A and B, we adopted a Bonnor-Ebert (BE) density profile for the initial cloud. A rigid rotation is adopted within the BE sphere, and a uniform magnetic field is imposed in the whole computational domain. In Cartesian coordinates, the direction of the global magnetic field is always parallel to the z-axis, while the rotation direction is inclined from the z-axis to the x-axis by an angle of θ_0.

The spatial resolution is the same among all simulations. The grid size and cell with of the $l = 1$ grid are

Table 2. Parameters and cloud physical quantities of initial clouds and calculation results

Model	θ_0	α_0	f	$M_{\rm cl}$	$R_{\rm cl}$	B_0	Ω_0	$R_{\rm disk}$	$R_{90\%}$	$M_{\rm disk}$	$M_{\rm sink}$
	(°)			($M_\odot$)	(au)	(10^{-5} G)	($10^{-13}\,{\rm s}^{-1}$)	(au)	(au)	($M_\odot$)	($M_\odot$)
A1	0							10.5	7.9	0.019	0.098
A2	10							28.8	13.8	0.044	0.089
A3	30							36.3	21.9	0.050	0.104
A4	45	0.4	2.0	1.0	5.9×10^3	43	1.5	50.1	22.9	0.060	0.100
A5	60							91.2	33.1	0.051	0.116
A6	80							69.2	22.9	0.048	0.124
A7	90							57.5	30.2	0.032	0.136
B1	0							27.5	15.1	0.090	0.222
B2	45	0.2	4.2	2.5	6.2×10^3	97	2.1	75.8	26.3	0.152	0.278
B3	90							109.6	28.8	0.141	0.296
B4	0							12.0	9.1	0.025	0.110
B5	45	0.4	2.1	1.2	6.2×10^3	48	1.5	57.5	26.3	0.068	0.127
B6	90							72.4	20.9	0.049	0.151
B7	0							9.5	6.9	0.011	0.084
B8	45	0.6	1.4	0.82	6.2×10^3	26	1.2	47.8	20.9	0.044	0.089
B9	90							60.3	21.9	0.016	0.117

NOTE— Column 1: model name; Columns 2 and 3: parameter θ_0 (the initial angle difference between the rotation axis and magnetic field) and α_0 (the ratio of thermal to gravitational energy); Column 4: density enhancement factor; Columns 5 and 6: initial cloud mass and radius; Columns 7 and 8: initial magnetic field strength and angular rotation rate; Columns 9–12: disk radius, radius of $M_{\rm enc} = 0.9 M_{\rm disk}$ (for definitions, see §4), disk mass, and protostellar mass at the end of the simulation ($t_{\rm ps} = 5000\,{\rm yr}$).

$L(1) = 1.9 \times 10^5\,{\rm au}$ and $h(1) = 2.9 \times 10^3\,{\rm au}$, respectively. We set the maximum grid level as $l = 14$ and the finest grid has $L(14) = 24\,{\rm au}$ and $h(14) = 0.36\,{\rm au}$, respectively.

To accelerate the time evolution, we adopt a sink cell technique (for details, see Machida et al. 2010; Machida & Hosokawa 2013). We set a threshold density $n_{\rm thr}$ and sink accretion radius $r_{\rm sink}$. In the collapsing cloud, we define the protostar formation epoch to begin when the gas density exceeds $n_{\rm thr}$. After protostar formation or sink creation, we remove the gas exceeding $n_{\rm thr}$ in the region of $r < r_{\rm sink}$ and add its mass to the gravitational potential of the protostar (Machida et al. 2010). In both Simulations A and B, we set $n_{\rm thr} = 10^{14}\,{\rm cm}^{-3}$ and $r_{\rm sink} = 0.5\,{\rm au}$, respectively. In the following, we explain details for each initial prestellar cloud in Simulations A and B. These parameters are summarized in Table 2.

3.1. *Simulations A*

We prepare the BE density profile $\rho_{\rm BE}(r)$ with the central density $n_{\rm c,0} = 5 \times 10^5\,{\rm cm}^{-3}$ and temperature $T_0 = 10\,{\rm K}$. To promote the cloud contraction, we enhance the density by f (density enhancement factor) as

$\rho(r) = f\rho_{\rm BE}(r)$ and adopted it as the density profile of the initial cloud. With $f = 2$, the mass and size of the initial cloud are $M_{\rm cl} = 1\,M_\odot$ and $R_{\rm cl} = 5.9 \times 10^3\,{\rm au}$, respectively. The magnetic field strength is adjusted to have a mass-to-flux ratio $\mu_0 = 3$, where μ_0 is normalized by the critical value $(4\pi^2 G)^{-1/2}$.[1] The strength of the uniform magnetic field is $B_0 = 4.3 \times 10^{-5}\,{\rm G}$. A rigid rotation of $\Omega_0 = 1.5 \times 10^{-13}\,{\rm s}^{-1}$ is adopted. With these settings, the ratio of thermal (α_0) and rotational (β_0) energies to the gravitational energy of the initial cloud are $\alpha_0 = 0.4$ and $\beta_0 = 0.02$, respectively. For the parameter θ_0, we adopt $\theta_0 = 0, 10, 30, 45, 60, 80,$ and $90°$. Thus, we executed seven simulations in total for Simulations A.

3.2. *Simulations B*

Since $\alpha_0 \propto c_{s,0}^2 M_{\rm cl}^{-1}$ (where $c_{s,0}$ is the sound speed and constant in the initial cloud), we can vary the value of parameter α_0 by changing the initial cloud density (or

---

[1] The mass-to-flux ratio becomes $\mu_0 = 3.797$ in the definition of Mouschovias & Spitzer (1976), in which the normalized factor $\sim (6.408\pi^2 G)^{1/2}$ is adopted.
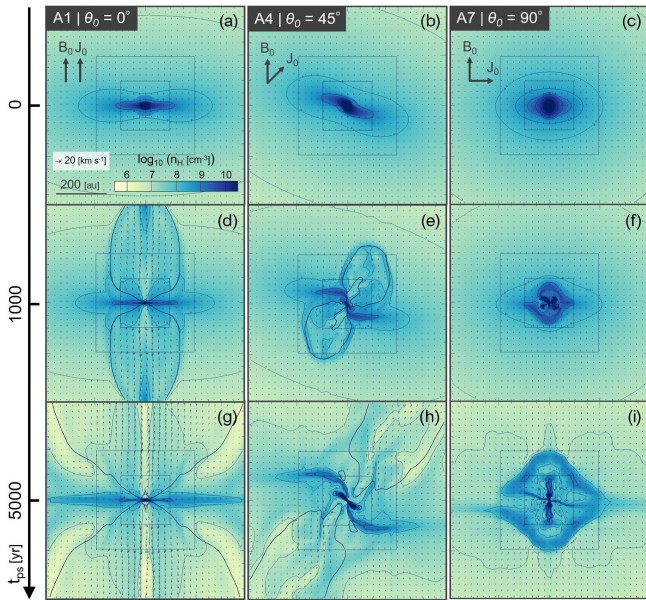
Figure 2. Density (color and contours) and velocity (arrows) distributions on the $y = 0$ plane for models A1 ($\theta_0 = 0°$; panels a, d, and g), A4 ($\theta_0 = 45°$; b, e, and h), and A7 ($\theta_0 = 90°$; c, f, and i) at $t_{ps} = 0$, 1000, and 5000 yr after protostar formation. The box size is 780 au. The squares in each panel represent a boundary of a nested grid.

initial cloud mass M_{cl}). The initial clouds prepared for Simulations B are almost the same as those for Simulations A but varying the density enhancement factor f in order to change the parameter α_0. All the models in Simulations B have the same cloud radius $R_{cl} = 6.2 \times 10^3$ au, which is slightly larger than in Simulations A. The mass differs in each model as listed in Table 2, as we changed the initial cloud density. The initial angular velocity Ω_0 and uniform magnetic field B_0 are adjusted to yield $\beta_0 = 0.02$ and $\mu_0 = 3$, respectively. Thus, models with different α_0 have the same non-dimensional parameters β_0 and μ_0 but different dimensional parameters Ω_0 and B_0.

4. RESULTS

As described in §3, we executed two types of simulations. Simulations A only changed the parameter θ_0 to focus on the effect of the angle difference between rotation axis and global field on the disk formation. Simulations B changed both the parameters θ_0 and α_0 in order to investigate the effect of the initial gravitational stability of the cloud.

4.1. *Simulations A: θ_0 dependence*

Figure 2 shows the time evolution for three models at $t_{ps} = 0$, 1000, and 5000 yr, in which $t_{ps} = 0$ at the sink creation epoch corresponding to the protostar formation. In the alignment model A1 ($\theta_0 = 0°$; the left column of Figure 2), the outflow gradually evolves and has
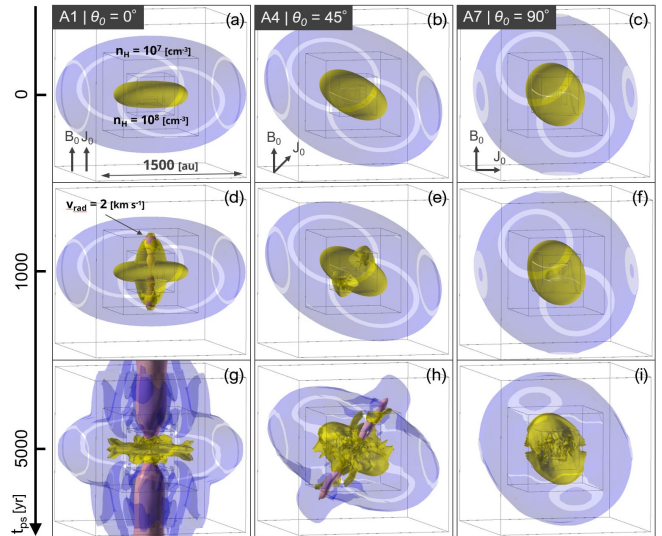

Figure 3. Three-dimensional structures for the same models as in Figure 2. We depict two isodensity contours of $n_H = 10^7$ cm^{-3} (purple) and 10^8 cm^{-3} (yellow) and one isovelocity contour of radial velocity $v_{rad} = 2$ km s^{-1} (red). The box size is 780 au. The squares in each panel denote a boundary of a nested grid. The white ellipse in each panel corresponds to the cutting plane of the boundary of the outermost grid surface.

a size of ~ 1000 au at $t_{ps} = 5000$ yr. Panels (d) and (g) show an oblate structure with a density of $\sim 10^8$ cm^{-3} corresponds to the pseudodisk. We confirm that the pseudodisk becomes thin with time. The high-density region ($\gtrsim 10^9$ cm^{-3}) corresponds to the rotationally-supported (or dense) disk.[2] The high-density disk becomes large with time. The bipolar outflow and geometrically thin and dense disk are clearly reproduced in the alignment model.

Next we focus on the misalignment model A4 ($\theta_0 = 45°$; the middle column of Figure 2). The outflow and disk system also appear in the misalignment model as seen in panels (e) and (h). However, the outflow direction is not aligned with the global (or initial) field direction that is parallel to the z-direction. The outflow direction is almost perpendicular to the disk direction, which indicates that the outflow propagates along the disk normal direction roughly corresponding to the initial rotation direction ($\boldsymbol{J_0}$). Thus the outflow propagation direction is not always coincident with the global B-field direction ($\boldsymbol{B_0}$). Misalignments between the inferred magnetic field direction and protostellar outflows

---

[2] Below we properly define the rotationally-supported disk with Figure 4. Before that time, we call the disk "the high-density disk" or simply "the disk". Actually, the high-density disk does roughly correspond to the rotationally-supported (or Keplerian) disk.

have been observed by Hull et al. (2013). In our simulations, the misalignment is clearly produced in the models with $\theta_0 \neq 0°$, in which the global field is not aligned with the initial rotation axis of the prestellar cloud core.

Figure 2 also indicates that the outflow in the misalignment model (middle column) is weaker than in the alignment model (left column). The effect of θ_0 on the outflow strength is discussed below. In addition, the misalignment model shows a complex structure of the pseudodisk. Figures 2(e) and (h) show a spiral structure that is formed from the pseudodisk twisted by rotation. The inner dense disk is enclosed by a twisted pseudodisk (Figure 2h).

Finally, we focus on the perpendicular model A7 ($\theta_0 = 90°$; the right column of Figure 2).[3] In this model, no strong outflow appears until the end of the calculation[4], while a large-sized dense disk, corresponding to the rotationally-supported disk (for details, see below), does appear. The normal direction of the dense disk corresponds to the rotation axis of the initial cloud core. In addition, the inner dense disk is wrapped by a relatively low-density spiral that corresponds to the pseudodisk twisted strongly by the rotation.

Figure 3 shows a time-sequence of structures in three dimensions for the same models. The figure indicates that the outflow (red isovelocity surface) and dense disk (yellow isodensity surface) system is enclosed by a less dense pseudodisk (purple isodensity surface) in the alignment (left column) and misalignment models (middle), while only a dense disk (yellow) is embedded in a nearly spherical structure (purple) in the perpendicular model (right). In addition, we can confirm that the pseudodisk (purple) is more distorted in the alignment models than in the perpendicular model. In other words, the misalignment models with $\theta_0 = 45$ and $90°$ have a nearly spherical structure (or a nearly spherical pseudodisk) around a geometrically thin and dense disk. This was also pointed out by Hennebelle & Ciardi (2009).

To compare the spatial scales between models with different θ_0, Figure 4 plots 3D views of the outflow, pseudodisk, and rotationally-supported disk at $t_{\rm ps} = 5000\,{\rm yr}$ for models with $\theta_0 = 0, 10, 45$, and $90°$. The figure indicates that, with the increment of θ_0, the outflow gradually weakens while the disk seems to increase its size. However, it is difficult to distinguish the rotationally-supported (or Keplerian) disk from the pseudodisk only with the density distribution, because the pseudodisk also has a disk-like structure in the high density region. To clearly identify the rotationally-supported disk in the computational domain, we imposed the following criteria:

(i) the number density is larger than $n > 10^{10}\,{\rm cm^{-3}}$,

(ii) the rotation velocity is greater than the radial velocity $|v_\phi| > f_{\rm rot}|v_{\rm rad}|$ by a factor $f_{\rm rot}$, where $f_{\rm rot} = 2$ is adopted,

(iii) the rotation velocity is in the range of $0.7 \leq |v_\phi/v_{\rm kep}| \leq 1.0$, where $v_{\rm kep} = [G(M_{\rm ps} + M_{\rm enc}(r))/r]^{1/2}$ is the Keplerian velocity.

Using the sink mass $M_{\rm sink}$[5], which is equated to the protostellar mass $M_{\rm ps}$, and the enclosed mass $M_{\rm enc}(r)$ within a radius r, we estimate the Keplerian velocity $v_{\rm kep}$. The procedure to identify the rotationally-supported disk is almost the same as that used in Joos et al. (2012). Note that although we imposed a lower limit of Keplerian velocity $0.7v_{\rm kep}$ in criterion (iii), the disk physical quantities such as mass and size do not significantly depend on the lower limit. The disk-like structure delineated by the green color in the middle and right panels of Figure 4 corresponds to the region where the criteria (i)–(iii) are satisfied. Thus, it corresponds to the rotationally-supported (or Keplerian) disk.

The right panels of Figure 4 show that the rotationally-supported disks have a spiral or complex structure near the disk outer edge. The spiral structure occupies a large extent especially in the misalignment models. The disk outer edge shows a high time variability and its structure changes in a short duration. Thus, a subtle structural change near the disk outer edge induces a significant change in the disk size. To exclude apparent or transient size changes of the disk, we defined the mass-weighted disk size, $R_{\rm disk}$, inside which the rotationally-supported-disk mass is contained. The radius of the mass-weighted disk is derived through the following procedure:

1) The total mass of the rotationally-supported disk, $M_{\rm tot}$, is derived by integrating over the entire disk,[6]

2) then, the mass of the rotationally-supported disk is radially integrated from the center until the integrated mass $M_{\rm disk}$ reaches $M_{\rm tot}$, and,

3) finally, the disk radius $R_{\rm disk}$ is determined as the radius inside which $M_{\rm tot}$ is contained.

The disk radius $R_{\rm disk}$ is represented by the solid circle in the right panels of Figure 4. From these panels, we

---

[3] The mirror symmetries in both the x- and z-directions are somewhat broken in Figures 2(f) and (i) but do not qualitatively affect the analyzed properties of the disk and outflow (see Appendix B).

[4] A very weak outflow does appear in the perpendicular model as shown in Figure 9.

[5] At every timestep, we estimated the gas falling onto the sink cell and added it to $M_{\rm sink}$.

[6] The rotationally-supported disk is identified with the criteria (i)–(iii).
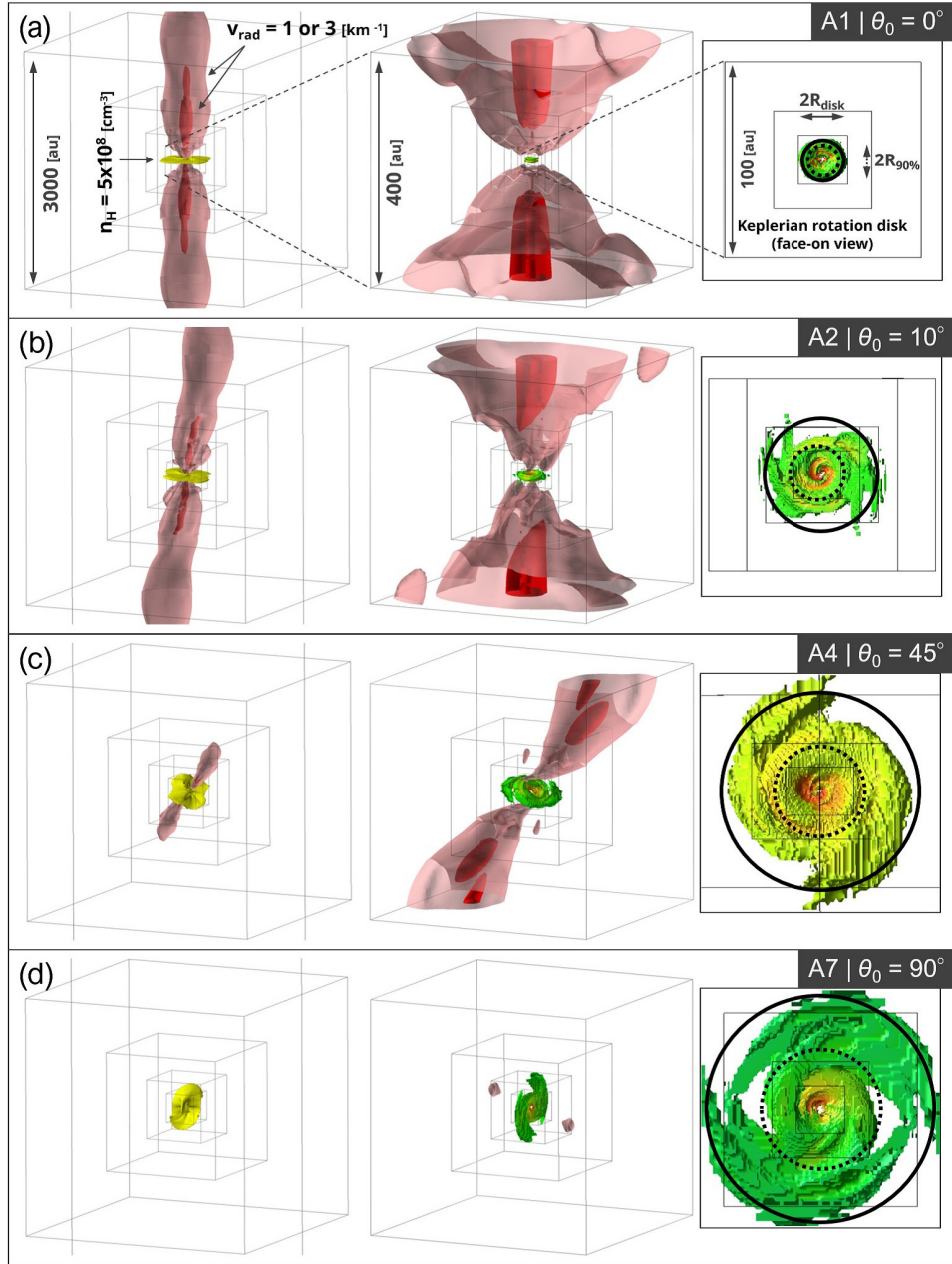
Figure 4. Three-dimensional view of the outflow, pseudodisk, and rotationally-supported disk with a box size of 3000 au (left column), 400 au (middle), and 100 au (right) for models A1 ($\theta_0 = 0°$; panel a), A2 ($\theta_0 = 10°$; b), A4 ($\theta_0 = 45°$; c), and A7 ($\theta_0 = 90°$; d) at $t_{ps} = 5000$ yr. The outflow is represented by the isovelocity surfaces of radial velocity $v_{rad} = 1$ (pink) and $3\,\mathrm{km\,s^{-1}}$ (red), respectively. In the left panels, the pseudodisk is represented by the yellow surface corresponding to an isodensity of $n_H = 5 \times 10^8\,\mathrm{cm^{-3}}$. In the middle and right panels, the rotationally-supported disk is plotted by a colored surface (the color represents the density on the disk surface). In each right panel, the viewing angle is adjusted to be face-on to the disk surface. The disk radii R_{disk} and $R_{90\%}$ are indicated by the solid and dashed circles, respectively. The nested squares in each panel indicate the boundaries of a nested grid.
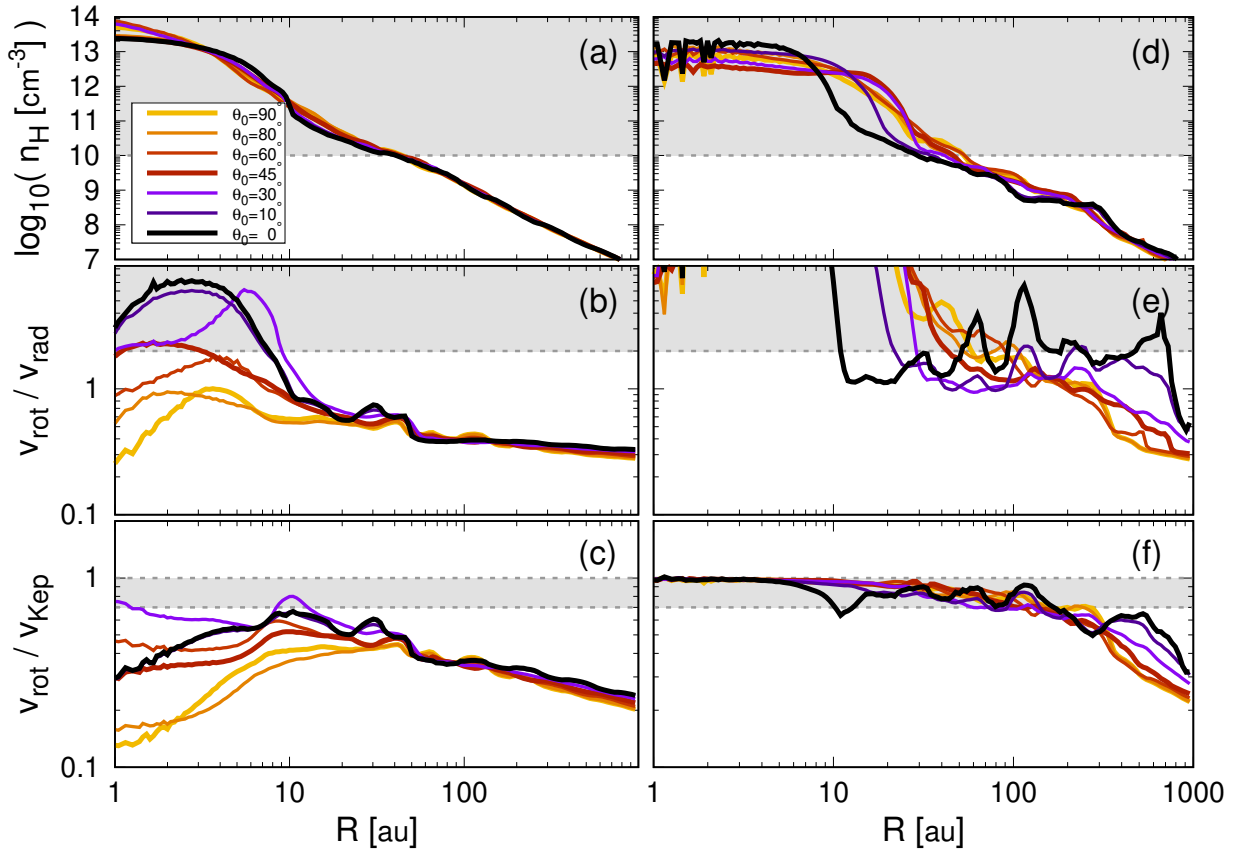
Figure 5. Radial profiles for all models in Simulations A at $t_{ps} = 0\,\mathrm{yr}$ (left panels) and $5000\,\mathrm{yr}$ (right), respectively: (panels a and d) number density, (b and e) ratio of the rotational to the radial velocity, and (c and f) ratio of the rotational to the Keplerian velocity. The gray zone in each panel corresponds to each criteria (i)–(iii) for identifying the rotationally-supported disk described in the text.

can confirm that the spiral or complex structure is contained within R_{disk}. We use R_{disk} as a typical radius of the rotationally-supported disk and simply call it the disk radius. In addition, we define another radius $R_{90\%}$ inside which 90% of the disk mass is contained. It is represented by the dashed circle in Figure 4. The size difference between R_{disk} and $R_{90\%}$ means that a large part of the disk mass is concentrated in the central region of the disk.

Figure 5 plots the radial profiles of number density, ratio of rotational to radial velocity, and ratio of rotational to Keplerian velocity for models A1–A7 at $t_{ps} = 0\,\mathrm{yr}$ (the protostar formation epoch) and $5000\,\mathrm{yr}$ (the end of the simulation), in which each value is azimuthally averaged. At the protostar formation epoch, the models have almost the same density distribution (Figure 5a). In addition, Figure 5(b) means that for all the models, the rotational velocity dominates or is comparable to the radial velocity even though the rotational velocity does not yet reach the Keplerian velocity. At the protostar formation epoch, all the models satisfy the disk identification criteria (i) $n > 10^{10}\,\mathrm{cm^{-3}}$ (Figure 5a) and some models satisfy the criteria (ii) $|v_\phi| > 2|v_{rad}|$ (Fig-

ure 5b). However, no model satisfies the third criteria (iii) $0.7 \leq |v_\phi/v_{Kep}| \leq 1.0$ (Figure 5c). Therefore, no Keplerian disk forms at this epoch.

On the other hand, at $t_{ps} = 5000\,\mathrm{yr}$, all the models satisfy the identification criteria for a rotationally-supported disk (i)–(iii), as seen in Figures 5(d–f). Especially, Figure 5(f) indicates that the rotation velocities are in rough agreement with the Keplerian velocity at $R \lesssim 10$–$100\,\mathrm{au}$. Hence, in all models, the Keplerian disk appears *after* protostar formation.

Next, we show the disk properties for all models in Simulations A. Top three rows in Figure 6 shows the disk radii R_{disk} and $R_{90\%}$, disk mass M_{disk}, and ratio of disk mass to protostellar mass M_{disk}/M_{ps} against the elapsed time after protostar formation (t_{ps}). The time evolution for the first 100 yr after protostar formation are plotted in the left panel, while those for 5000 yr (by the end of the simulations) are plotted in the right panel. In previous studies, Matsumoto & Tomisaka (2004) showed that the disk is larger in the aligned case ($\theta_0 = 0°$) than in the perpendicular case ($\theta_0 = 90°$). On the other hand, Joos et al. (2012) showed the opposite result; the disk is larger in the misaligned case ($\theta_0 \neq 0°$) than in the aligned case.
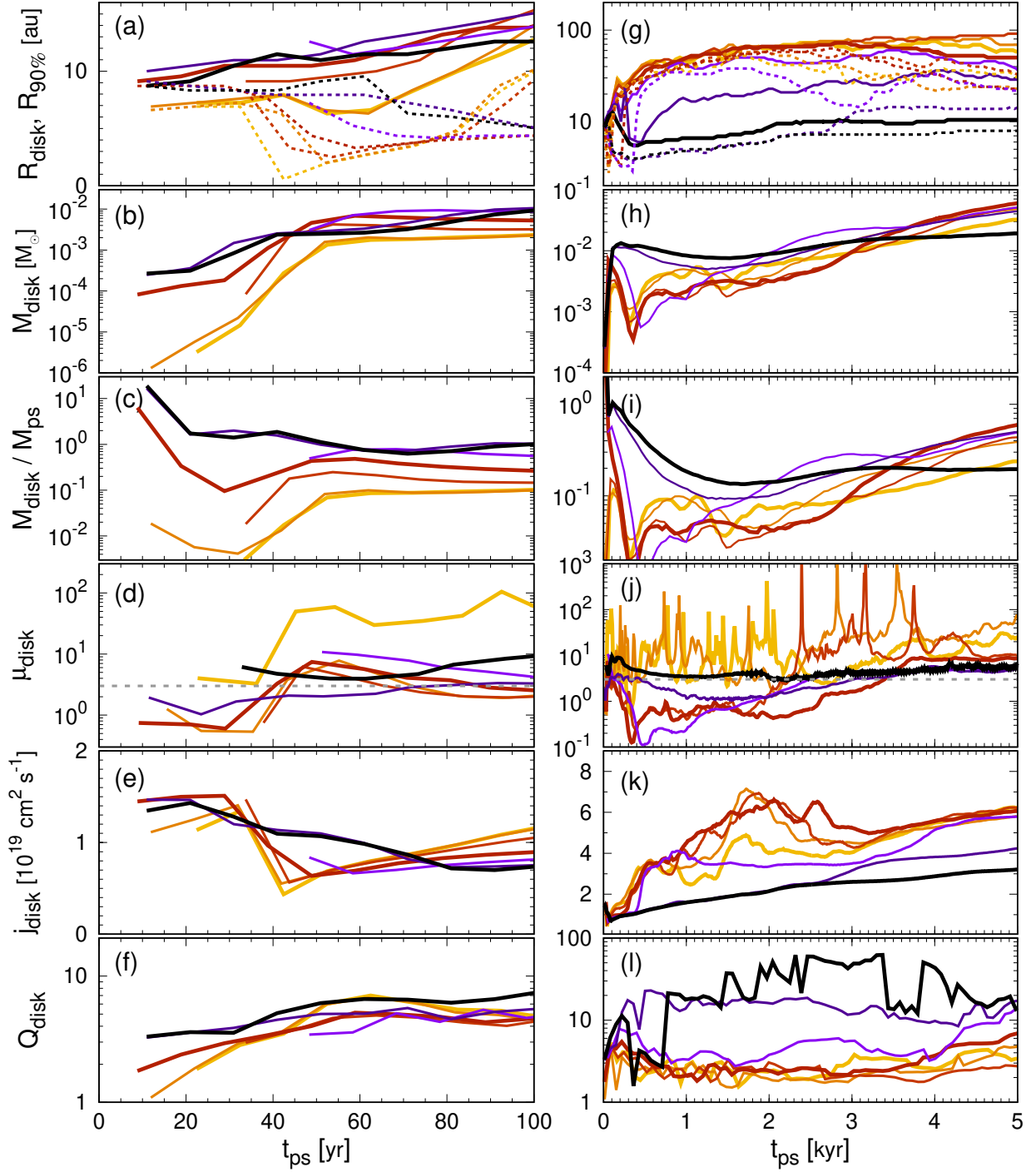
Figure 6. Time evolution of disk properties for all models in Simulations A during the first 100 yr (left panels) and 5000 yr (right) after the protostar formation, respectively: (panels a and g) radius of $M = M_{tot}$ (R_{disk}, solid lines) and $M = 0.9M_{tot}$ ($R_{90\%}$, dotted lines), (b and h) disk mass, (c and i) ratio of disk mass to protostellar mass, (d and j) magnetization (or normalized mass-to-flux ratio), (e and k) specific angular momentum, and (f and l) Toomre Q parameter averaged over the disk. The dashed line in panel (d) plots the initial mass-to-flux ratio, $\mu_0 = 3$.

The disk evolution for the first $\sim 600\,\mathrm{yr}$ was calculated in Matsumoto & Tomisaka (2004), while up to $\sim 5000\,\mathrm{yr}$ were investigated by Joos et al. (2012). The parameters of initial clouds also differ between two studies. Here we investigate both a short and long timescale of the disk evolution, so we prepared two sets of panels in Figure 6.

During the very early phase after protostar formation ($t_{\mathrm{ps}} < 100\,\mathrm{yr}$), the disk tends to have a small radius and small mass in models with a large θ_0 compared to models with a small θ_0. The disk radius R_{disk} for the model with $\theta_0 = 90°$ is the smallest among the models for $t_{\mathrm{ps}} \lesssim 100\,\mathrm{yr}$, while it becomes the largest after that (Figure 6a). The radii of $M = 0.9\,M_{\mathrm{tot}}$, $R_{90\%}$, are smaller than R_{disk} but the dependence of $R_{90\%}$ evolution on θ_0 is similar to R_{disk}. The disk mass for the model with $\theta_0 = 90°$ is also the smallest for $t_{\mathrm{ps}} \lesssim 100\,\mathrm{yr}$ (Figure 6b). In addition, Figure 6(c) indicates that the disk mass for the model with $\theta_0 \geq 80°$ is one or two orders of magnitude less than the protostellar mass, while the disk mass for models with $\theta_0 \leq 30°$ is comparable to the protostellar mass. Thus, during the early phase, the disk radius and mass for the alignment model are larger than that for the perpendicular model, which agrees well with the results of Matsumoto & Tomisaka (2004).

Both the radius- and mass-magnitude relations show a variation with time. Figure 6(g) shows that the disk radius for the alignment model is as small as $r_{\mathrm{disk}} \sim 10\,\mathrm{au}$ by the end of the simulation, which agrees with Machida et al. (2014) and Machida & Basu (2019). On the other hand, during $t_{\mathrm{ps}} \lesssim 5000\,\mathrm{yr}$, the disk radius increases to 10–100 au in the misalignment models. Thus, the radius-magnitude relation is reversed at these times. In Figure 6(g), the dependence of disk radius on θ_0 is also the same for R_{disk} and $R_{90\%}$ (see also the final values in Table 2). Figures 6(h) shows that the magnitude relation of the disk mass is also reversed at $t_{\mathrm{ps}} \sim 3000\,\mathrm{yr}$, as the disk mass for the perpendicular model becomes the largest and that for the alignment model becomes the smallest among the models. This tendency is in good agreement with Joos et al. (2012) and Hennebelle & Ciardi (2009), who claimed that the radius and mass are maximized for the perpendicular case.

Figures 6(d) and (j) show the time evolution of the magnetization (normalized mass-to-flux ratio) in the disk, μ_{disk}. The magnetization in the disk is determined by the balance between the amplification and dissipation of the magnetic field. The magnetic field in the disk is amplified by the cloud contraction and the accretion of magnetized matter, while it dissipates by Ohmic dissipation. In the early phase, μ_{disk} is lower in misaligned models. Note that the mass-to-flux ratio of the perpendicular model ($\theta_0 = 90°$) is largest among models, which may be attributed to the geometry of the accretion in the early accretion phase (Tsukamoto et al. 2018). In the later phase, μ_{disk} is lower with decreasing θ_0. Although the time evolution of μ_{disk} is not very simple, the disk tends to have a weak magnetic field when the

disk is large or massive. This is natural because the dissipation of magnetic field is efficient in the high-density disk region.

The angular momentum of the disk is carried away by the outflows and magnetic field. To quantify the relative importance of the mechanisms, we measure the integral fluxes of angular momentum (for details, see Section 5.4.1 in Joos et al. 2012) carried away by the magnetic torque,

$$F_{\mathrm{mag}} = \left| \int_{\mathrm{disk}} r \frac{B_\phi}{4\pi} \mathbf{B} \cdot d\mathbf{S} \right| \; , \tag{1}$$

carried away by the outflows,

$$F_{\mathrm{out}} = \left| \int_{\mathrm{disk}} \rho r v_\phi \mathbf{v} \cdot d\mathbf{S} \right| \; , \; \text{for } \mathbf{v} \cdot d\mathbf{S} > 0, \tag{2}$$

and carried in by the accretion flow,

$$F_{\mathrm{in}} = \left| \int_{\mathrm{disk}} \rho r v_\phi \mathbf{v} \cdot d\mathbf{S} \right| \; , \; \text{for } \mathbf{v} \cdot d\mathbf{S} < 0. \tag{3}$$

We calculate the total fluxes over the surface S, of a cylinder having a radius corresponding to the Keplerian disk, in which the disk rotation axis is adopted as the axis of the cylinder. The height of the cylinder is set to enclose the whole region of the disk. Thus, both the axis and size of the cylinder change with time. Figure 7 plots the outgoing fluxes of the angular momentum normalized by the incoming flux. Although the angular momentum transferred by the outflow sometimes dominates that by the magnetic torque, the magnetic torque contributes mainly to the angular momentum transfer. Thus, the magnetic torque (i.e., magnetic braking) is a more important factor for disk formation, which is consistent with Joos et al. (2012). These incoming and outgoing fluxes should primarily determine the total angular momentum of the disk (Figures 6e and k) and the disk properties. We tentatively calculated the time evolution of the angular momentum assuming a cylindrical surface, as according to Joos et al. (2012). However, it is very difficult to more precisely estimate the angular momentum transported from the central region where other mechanisms such as gravitational and thermal pressure torques should play a role for transporting the angular momentum. Although further detailed analysis of the disk angular momentum (transport) is necessary, it is beyond the scope of this study.

To confirm the disk stability, we estimate the mass-weighted Toomre Q parameter (Toomre 1964) which is averaged over the entire disk $R < R_{\mathrm{disk}}$ as

$$Q_{\mathrm{disk}} = \frac{\int_{\mathrm{disk}} (c_{\mathrm{s}} \kappa)/(\pi G \Sigma) \Sigma \, dS}{\int_{\mathrm{disk}} \Sigma \, dS} \; , \tag{4}$$

where c_s is the sound speed, G is the gravitational constant, Σ is the surface density, and

$$\kappa = 4\Omega^2 + r \frac{d\Omega^2}{dR} \tag{5}$$
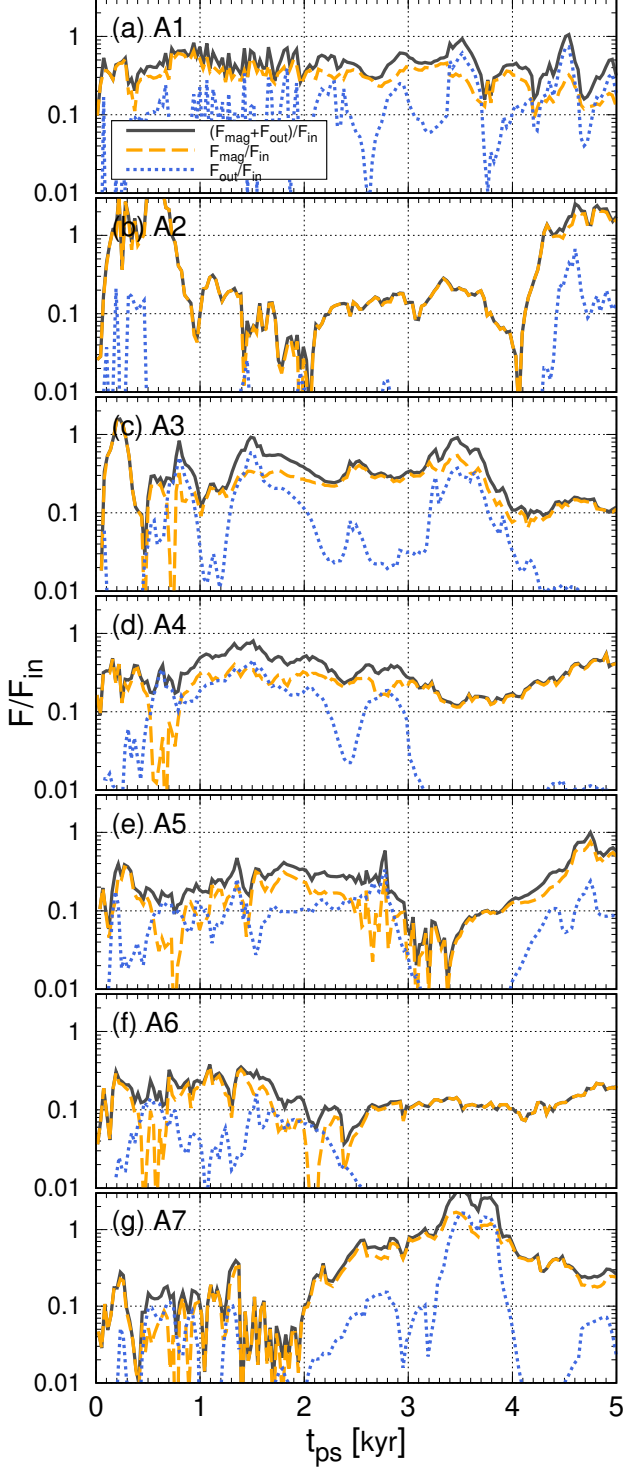
Figure 7. Time evolution of the outgoing fluxes of the angular momentum (Equations 1 and 2) normalized by the incoming flux (Equation 3) for all models in Simulations A until 5000 yr after the protostar formation: $(F_{\mathrm{mag}}+F_{\mathrm{out}})/F_{\mathrm{in}}$ (solid lines), $F_{\mathrm{mag}}/F_{\mathrm{in}}$ (dashed), and $F_{\mathrm{out}}/F_{\mathrm{in}}$ (dotted).
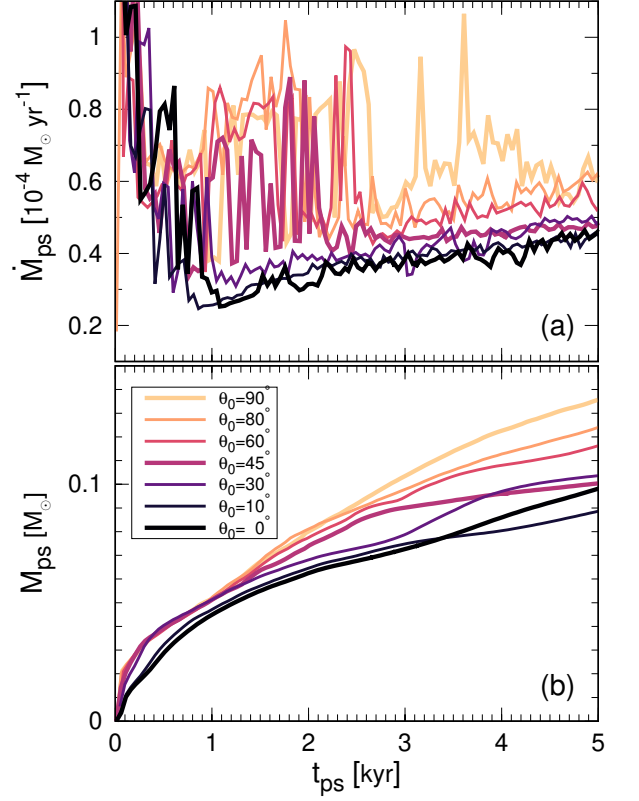
Figure 8. Mass accretion rate (top panel) and protostellar mass (bottom) versus the elapsed time after protostar formation for all models in Simulations A.
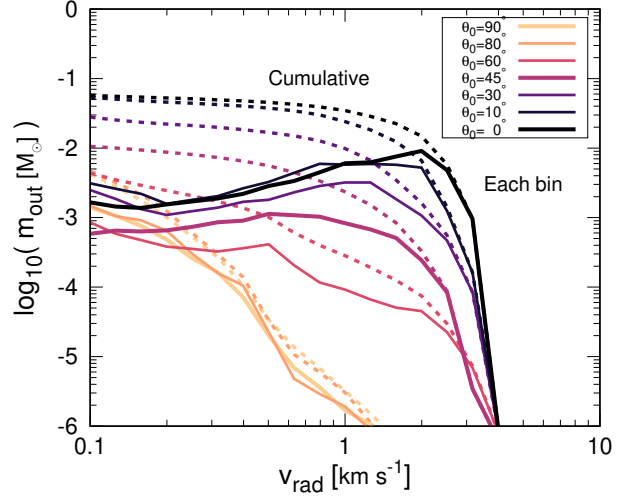
Figure 9. Mass versus the radial velocity at the end of the simulation ($t_{\mathrm{ps}} = 5000\,\mathrm{yr}$) for all models in Simulations A. Solid and broken lines plot the mass in each velocity bin (m_{out}; Equation 6) and the cumulative mass (M_{out}; Equation 7), respectively.

is the epicyclic frequency, in which Ω is the angular velocity. Figures 6(f) and (l) plot the time evolution of $Q_{\rm disk}$. Note that the Q parameter estimated here is an average of the entire Keplerian disk, and not a local quantity. However, it is plausible to use it to discuss the gravitational instability among the models. During the first 100 yr, $Q_{\rm disk}$ gradually increases, which means that the disk gradually stabilizes. After $Q_{\rm disk}$ has a local peak around $t_{\rm ps} \simeq 100\,{\rm yr}$ (Figure 6l), it decreases with time in the misalignment models ($\theta_0 \neq 0°$). On the other hand, we can see a strong oscillation in the Q parameter for the aligned model $\theta_0 = 0°$, as seen in Tomida et al. (2017). The spiral arm induced by the disk gravitational instability becomes clear (Figure 4) as the disk size increases (Figure 6g). We can see clear spiral patters in the models with large θ_0 that have smaller $Q_{\rm disk}$ (Figures 6f and l).

Figure 8 shows the mass accretion rate and protostellar mass for all models plotted against the elapsed time. The top panel shows that the time variation of the mass accretion rate is greater in the misalignment models than in the alignment model. This is consistent with the θ_0-dependence of the disk gravitational instability expected from the time evolution of Q parameter (Figures 6f and l). The bottom panel indicates that the protostellar mass is greater in the misalignment models than in the alignment model. Both panels indicate that the mass accretion rate tends to be high when the initial angle difference θ_0 is large. Figures 6 and 8 show that both the protostellar mass and disk mass are greater in the misalignment models than in the alignment model.

The total mass flowing into the central region is roughly the same among the models, but the alignment model actually has a massive outflow that compensates for the total mass flowing into the central region. Figure 9 shows the outgoing mass plotted against the radial velocity at $t_{\rm ps} = 5000\,{\rm yr}$ for all models in Simulations A. We calculate masses in every bin of the radial velocity as

$$m_{\rm out}(v_{\rm rad}) = \int_{v_{\rm rad}-\Delta v}^{v_{\rm rad}+\Delta v} \rho\, dV \ , \qquad (6)$$

and cumulative masses

$$M_{\rm out}(v_{\rm rad}) = \int_{v_{\rm rad}}^{\infty} \rho\, dV \ . \qquad (7)$$

The figure indicates that the outflow mass (e.g., with $v_{\rm rad} \gtrsim 0.2\,{\rm km\,s^{-1}}$) for the alignment model is about two orders of magnitude greater than that for the perpendicular model. Thus, a large part of the outgoing mass is removed from the central region by the outflow. Figure 9 also indicates that the outflow mass decreases with increasing θ_0. Our results are consistent with Li et al. (2013) who claimed that the outflow becomes stronger in the alignment model than the misalignment one.

4.2. *Simulations B: θ_0 and α_0 dependences*

This subsection shows the results of Simulations B. Tsukamoto et al. (2018) pointed out that initial cloud stability, which can be represented by the parameter α_0, affects the disk formation. When the prestellar cloud is in a highly unstable state, the cloud rapidly collapses while maintaining a nearly spherical configuration. In such a cloud, the mass accretion rate becomes high (Matsushita et al. 2017). On the other hand, when the prestellar cloud is in a nearly stable state, the gas fluid near the rotation axis, which has a relatively small angular momentum, preferentially falls onto the central region. For these reasons, Tsukamoto et al. (2018) claimed that a relatively large-sized disk forms in the cloud with a small α_0. However, as described above, since Tsukamoto et al. (2018) only calculated a very early phase of the disk formation, we could not know whether a large-sized disk really forms in a highly unstable state. To investigate the effect of the initial cloud stability on the disk formation, we prepared the set of models in Simulations B.

As listed in Table 2, for the models of Simulations B, we changed both the parameters θ_0 and α_0 in order to investigate the effects of the angle difference and gravitational stability on disk formation. Although we adopted various values of θ_0 in Simulations A, we used only three different angles $\theta_0 = 0°$ (alignment model), $45°$ (misalignment), and $90°$ (perpendicular) for Simulations B. We also adopted three different values for α_0 ($= 0.2$, 0.4, and 0.6). For these models, we also calculated the cloud evolution until $t_{\rm ps} = 5000\,{\rm yr}$.

The calculation results for all models in Simulations B are plotted in Figure 10. We can see the emergence of a strong outflow in the alignment models with $\theta_0 = 0°$ (bottom panels), while a weak outflow appears in the misalignment models with $\theta_0 = 45°$ (middle). On the other hand, the perpendicular models with $\theta_0 = 90°$ (top) did not show a noticeable outflow by the end of the simulation. This clearly shows that the outflow strength weakens with increments of θ_0, as shown in §4.1. Figure 10 also indicates that the outflow strength depends weakly on α_0, in which a relatively strong outflow appears in the model with a smaller α_0. Thus, a strong outflow develops in an initially unstable cloud as pointed out by Matsushita et al. (2017, 2018).

In Figure 11, we quantitatively compare the disk properties for the models in Simulations B, as in Figure 6. The time evolution of each quantity is plotted during $t_{\rm ps} = 1000$–$5000\,{\rm yr}$. Figures 11(a)–(c) plot the time evolution of the disk radii $R_{\rm disk}$ and $R_{90\%}$ and indicate that the disk size increases as the angle difference θ_0 increases (see also §4.1). The figure also shows that the disk size decreases as the parameter α_0 increases, while the difference in the disk size among models with different α_0 is not very large. Model B3, with the smallest α_0 ($= 0.2$) and the largest θ_0 ($= 90°$), has the largest disk, while model B7 with the largest α_0 ($= 0.6$) and the smallest θ_0 ($= 0°$) has the smallest disk. The disk size at the
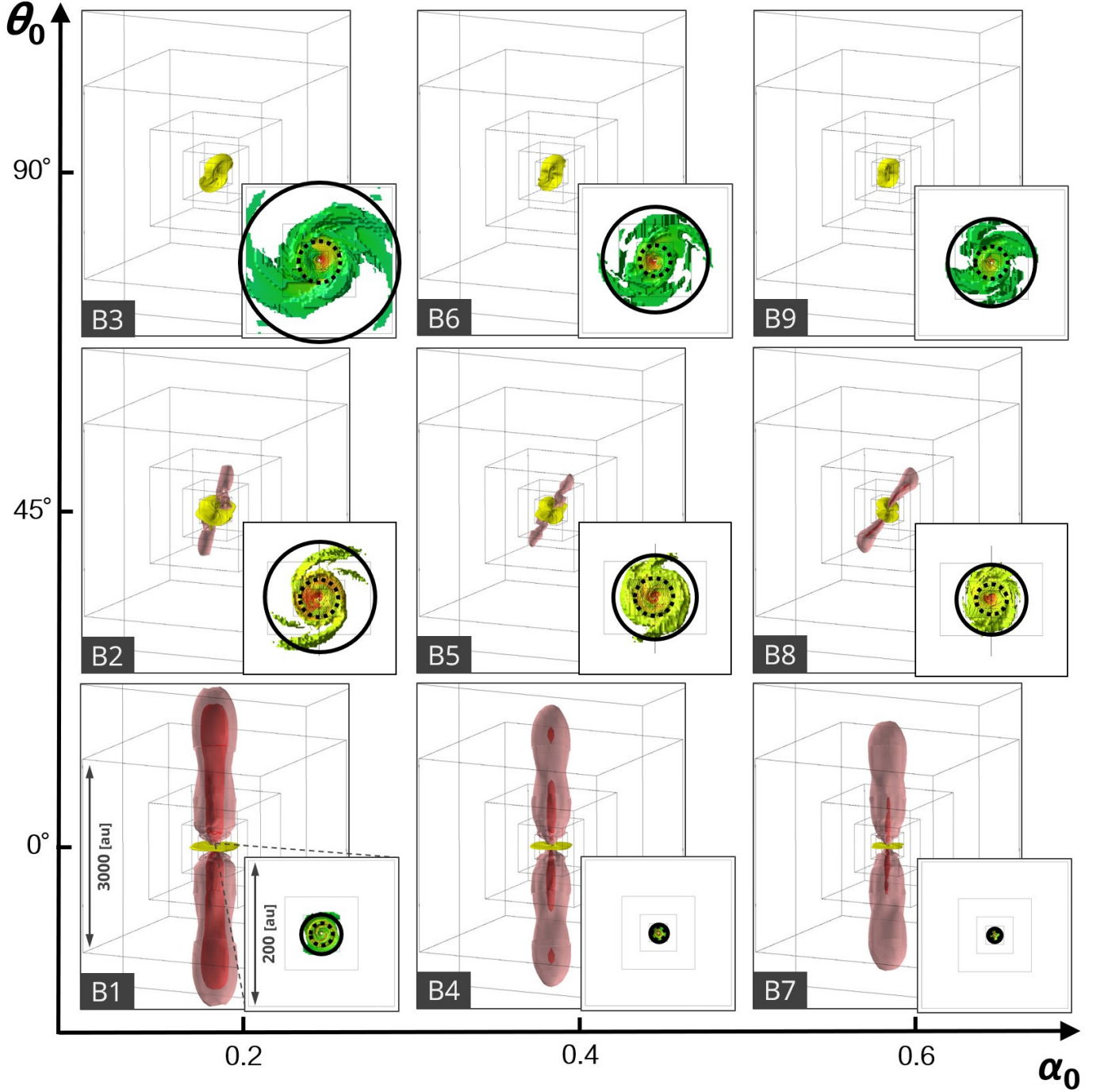
Figure 10. Three-dimensional view of the outflow, pseudodisk, and rotationally-supported disk at $t_{\rm ps} = 5000\,{\rm yr}$ with a box size of $3000\,{\rm au}$ and $200\,{\rm au}$ (inset) for all models in Simulations B. In each inserted figure (bottom right corner), the viewing angle is adjusted to become face-on to the disk surface. Each model (B1–B9) is placed on the parameter space of α_0 (horizontal axis) and θ_0 (vertical axis), in which the model name is described in the left bottom corner. In each panel, the outflow is represented by the isovelocity surfaces of $v_{\rm rad} = 1$ (pink) and $3\,{\rm km\,s^{-1}}$ (red), respectively. The pseudodisk is represented by the yellow surface corresponding to an isodensity of $n_{\rm H} = 5 \times 10^8\,{\rm cm^{-3}}$. In the inserted figure, the rotationally-supported disk is plotted in colors that represent the density on the disk surface. The solid and dashed circles are the disk radii $R_{\rm disk}$ and $R_{90\%}$, respectively. The nested squares in each panel indicate the boundaries of a nested grid.
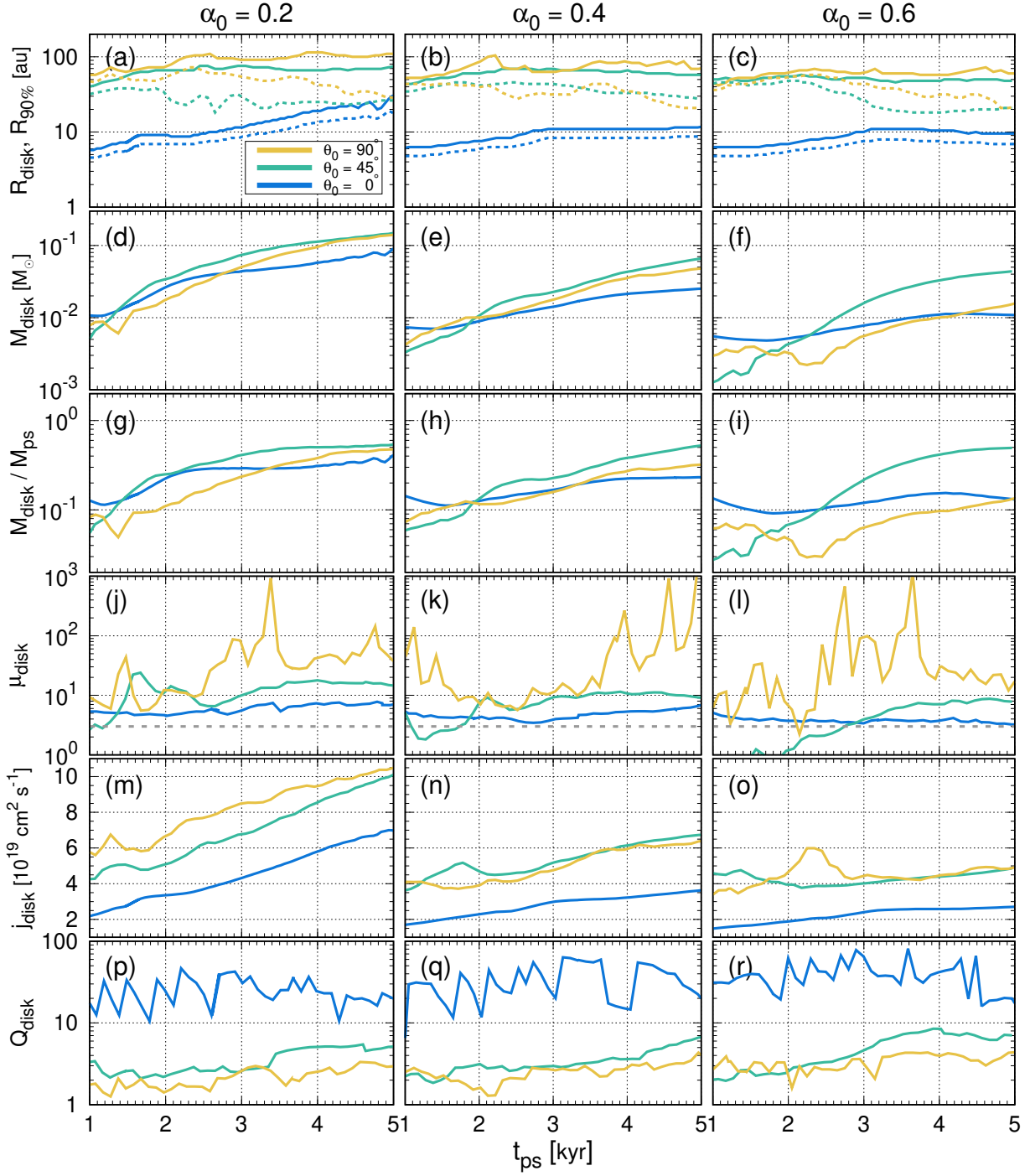
Figure 11. Time evolution of the disk and protostar properties for all models in Simulations B against the elapsed time during $t_{ps} = 1000$–$5000\,\mathrm{yr}$: (panels a, b, c) radii R_{disk} (solid) and $R_{90\%}$ (dotted), (d, e, f) disk mass, (g, h, i) ratio of disk mass to protostellar mass, (j, k, l) magnetization (normalized mass-to-flux ratio), (m, n, o) specific angular momentum, and (p, q, r) Toomre Q parameter averaged over the entire disk. The dashed line in the panels (j), (k) and (l) plots the initial mass-to-flux ratio, $\mu_0 = 3$.
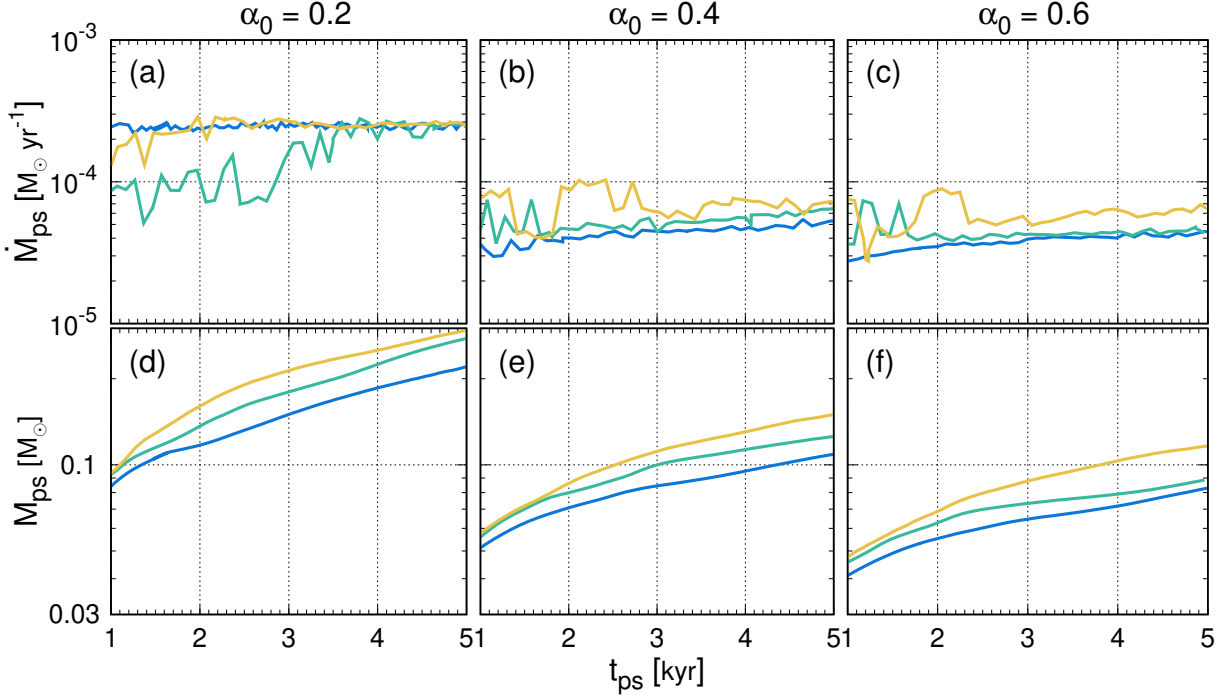
Figure 12. Mass accretion rate (top panels) and protostellar mass (bottom panels) versus the elapsed time after protostar formation for all models in Simulations B.

end of the simulations are plotted as the solid circle in Figure 10.

Figures 11(d)–(f) plot the time evolution of the disk mass. Also, the disks in the misalignment and perpendicular models tend to have a greater mass than in the alignment models. However, the difference is not very clear, and the disk mass–magnitude relation depends on the evolutionary stage. For example, at the end of the simulation ($t_{\rm ps} = 5000\,{\rm yr}$), the model with $\theta_0 = 90°$ has the most massive disk among models with $\alpha_0 = 0.2$, while the disks in the models with $\theta_0 = 45°$ are the most massive in the clouds with $\alpha_0 = 0.4$ and 0.6.

Figures 12(d)–(f) show that the protostellar mass is greater in the models with a smaller α_0 than in the models with larger α_0. As shown in Matsushita et al. (2017), the mass accretion rate is proportional to $\alpha_0^{-3/2}$. Thus, it is natural that the model with a small α_0 has greater protostellar and disk masses, because a large amount of gas falls into the central region for a short duration (Figures 12(a)–(c)). In addition, when the parameter α_0 is fixed, Figure 12(d)–(f) indicate that the protostellar mass increases with increasing θ_0. Since a part of the mass flowing to the central region is sent back to the surrounding cloud by the outflow, we need to consider the effect of the outflow when considering the total mass falling into the central region, as described in §4.1. The parameter α_0 regulates the mass and angular momentum flowing to the central region, while the parameter θ_0 determines the efficiency of the outward transport of the angular momentum. Since some factors are mixed

in the protostar and disk formation process, it is hard to tell which effect is most important for disk formation.

Figures 11(j)–(l) show the magnetization (or the normalized mass-to-flux ratio) of the disk. In addition to the dependence on θ_0 discussed in §4.1, $\mu_{\rm disk}$ becomes slightly lower with increasing α_0 throughout the simulation. This dependence is considered to reflect the difference of the total magnetic flux introduced in the disk. The accretion rate of both mass and magnetic flux is high in the model with lower α_0, which results in a disk with a strong magnetic field, i.e., low mass-to-flux ratio.

The specific angular momentum is a useful index for comparison of disks among models. Figures 11(m)–(o) indicate that the specific angular momentum is greater in the misalignment model than in the alignment model. Independent of α_0, there exists a significant different between the alignment and misalignment models. Figure 13 plots the angular momentum fluxes carried away by the magnetic torque and outflows normalized by the flux carried in by the accretion flow. The ratio of the outgoing flux to the incoming one is slightly lower in the misalignment model than in the alignment model. Furthermore, the normalized flux increases with increasing α_0. The dependence on these two parameters results in the differences of the specific angular momentum among models (Figures 11m–o).

Figures 11(p)–(r) plot the Toomre parameter $Q_{\rm disk}$. As seen in models of Simulations A, $Q_{\rm disk}$ decreases as θ_0 increases. In addition, $Q_{\rm disk}$ slightly decreases as α_0
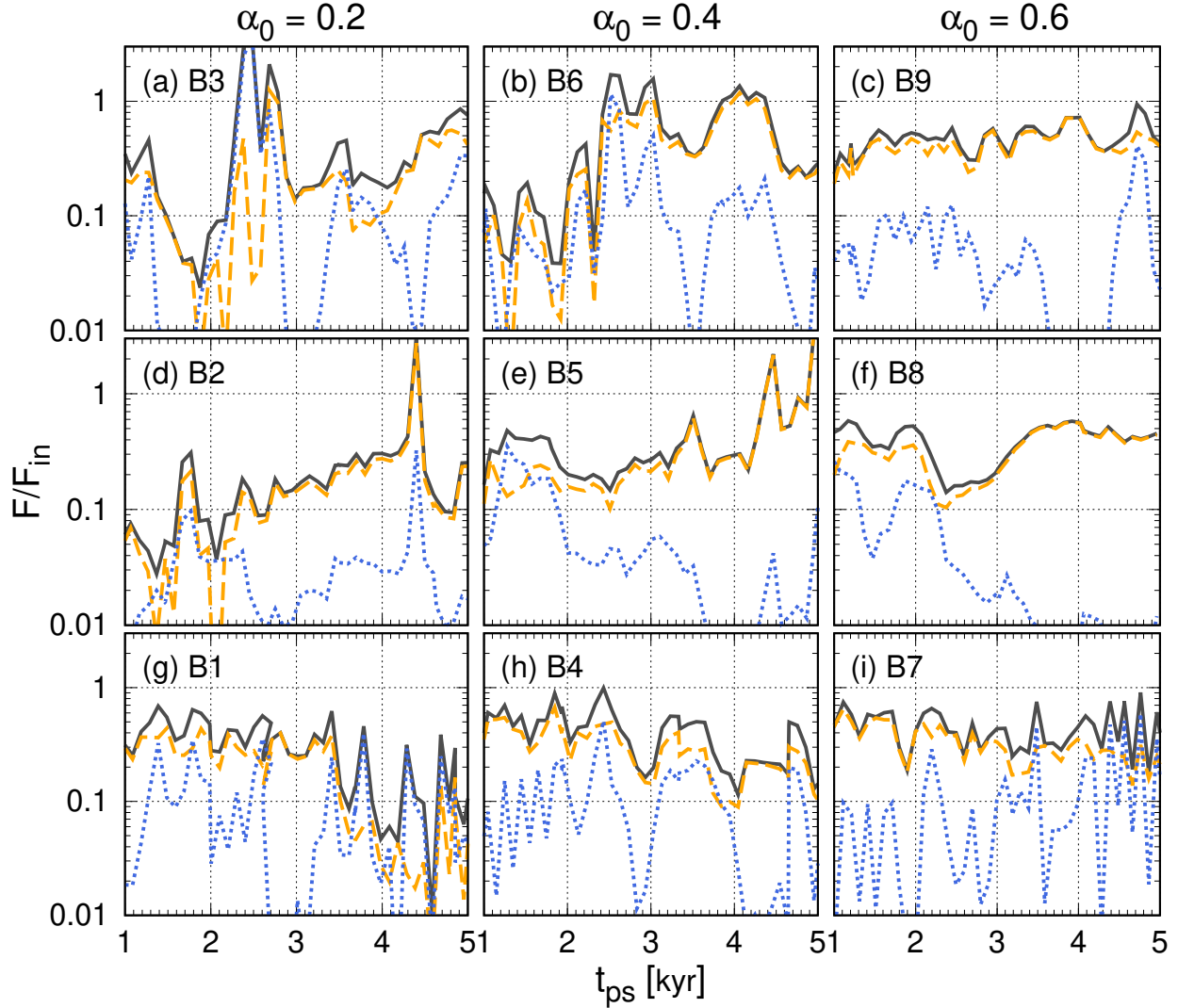
Figure 13. Same as in Figure 7 but for all models in Simulations B. $(F_{\rm mag} + F_{\rm out})/F_{\rm in}$ (solid lines), $F_{\rm mag}/F_{\rm in}$ (dashed), and $F_{\rm out}/F_{\rm in}$ (dotted) are plotted against the elapsed time after protostar formation.

decreases. For example, Figure 10 shows that the spiral arm appears most strongly in model B3. It is natural that a high mass accretion rate (or small α_0) tends to produce a gravitationally unstable disk associated with apparent spiral arms. The dependence of the mass accretion rate and protostellar mass on the parameters α_0 and θ_0 can be confirmed in Figure 12.

Figure 14 shows the outgoing mass plotted against the radial velocity at $t_{\rm ps} = 5000\,{\rm yr}$. In addition to the mass in each velocity bin, the cumulative mass is also shown. The cumulative masses with $v_{\rm rad} \geq 0.1\,{\rm km\,s^{-1}}$ for the alignment models ($\theta_0 = 0°$) are $M_{\rm out} \sim 0.14$, 0.068, and 0.046 $M_\odot$ for $\alpha_0 = 0.2$, 0.4, and 0.6, respectively. The masses for the misalignment models ($\theta_0 = 45°$) are $M_{\rm out} \sim 0.038$, 0.015, and 0.011 $M_\odot$, which are several times lesser than those for the alignment models. In addition, the masses for the perpendicular models

($\theta_0 = 90°$) are $M_{\rm out} \sim 0.018$, 0.0047, and 0.0037 $M_\odot$, which are about one orders of magnitude less than those for the alignment models. Furthermore, the alignment models have the high-velocity component of the outflow ($v_{\rm rad} > 1\,{\rm km\,s^{-1}}$), while the outflow for the perpendicular models have only the slow-velocity component $v_{\rm rad} \lesssim 1\,{\rm km\,s^{-1}}$.

The cumulative mass $M_{\rm out} \sim 0.1\,M_\odot$ is comparable to the disk and protostellar masses for the alignment models. Thus, the outflow plays a significant role in the disk formation in these cases. On the other hand, for the perpendicular models, the outflow mass $M_{\rm outflow} \ll 0.01\,M_\odot$ is much less than the protostellar and disk masses. In this case, the outflow does not play a significant role in the disk formation, as described by Li et al. (2013).
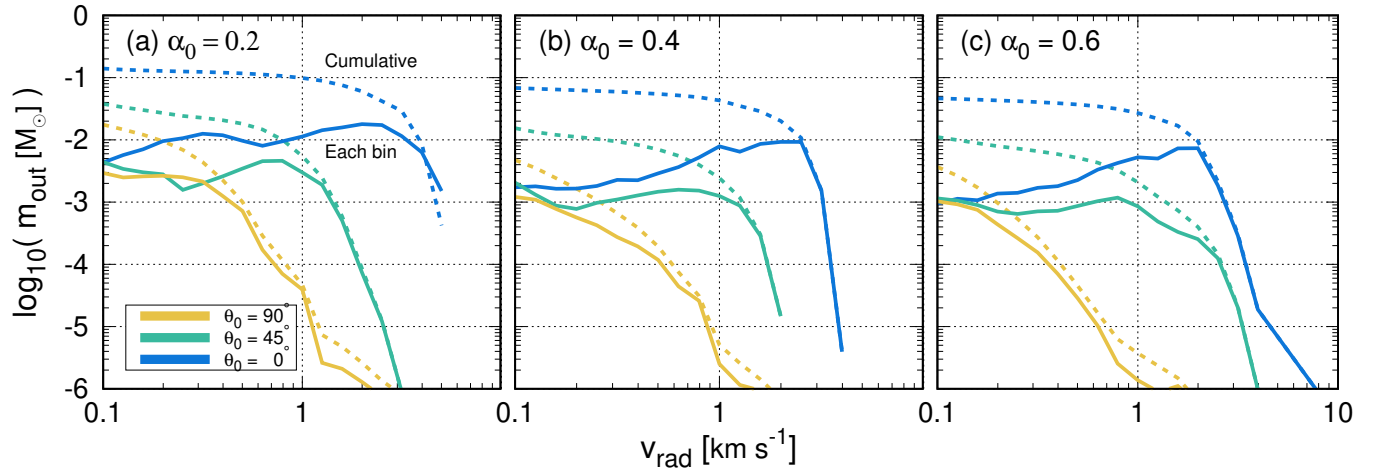
Figure 14. Mass versus radial velocity at the end of the simulation ($t_{\rm ps} = 5000\,{\rm yr}$) for (panel a) models B1–B3 (with $\alpha_0 = 0.2$), (b) B4–B6 (0.4), and (c) B7–B9 (0.6). Solid and broken lines plot the mass in each velocity bin and the cumulative mass, respectively.

Figure 10 shows that, in addition to θ_0, the initial cloud stability α_0 is a significant factor to determine the efficiency of the angular momentum transfer. In an initially nearly stable cloud, which has a large α_0, the angular momentum is excessively transferred by magnetic braking and/or outflow and a small-sized disk appears. On the other hand, in an initial unstable cloud with a small α_0, a massive disk tends to appear because the gas and angular momentum are advected to the central region in a short duration.

5. DISCUSSION

In §4, we showed that, in the very early accretion phase (Figure 6a), the rotationally-supported disk is larger in the alignment model ($\theta_0 = 0°$) than in the misalignment models ($\theta_0 \neq 0°$). However, the disk growth rate is greater in the misalignment models than in the alignment models. Thus, in the later accretion phase, the disk size in the misalignment models exceeds that in the alignment models (Figures 6e and 11a–c). At the end of the simulation ($t_{\rm ps} = 5000\,{\rm yr}$), the disks in the misalignment models are about 3–5 times larger than that in the alignment models.

We can also see a similar trend in the disk mass (Figures 6c, 6h, and 11g–i). The disk is more massive in the alignment models than in the misalignment models in the very early accretion phase, while the disk becomes more massive in the misalignment models than in the alignment models in the later accretion phase. The disk radius and mass at $t_{\rm ps} = 5000\,{\rm yr}$ for all the models are described in Table 1. In summary, a relatively large-sized disk is seen in the alignment models only in the early accretion phase, while the disk in the misalignment models grows and its size becomes larger than in the alignment models in the later accretion phase. Our simulations showed that the relation between the disk

size and mass among models is changed during the mass accretion phase.

Joos et al. (2012) pointed out that a fan-shaped configuration of magnetic field is finally realized in the alignment case. As described in §2, the moment of inertia is larger in the fan-shaped configuration than in the spiral configuration which is realized in the perpendicular case. Thus, the angular momentum is effectively transferred in the alignment case if the fan-shaped configuration is realized with $\theta_0 = 0°$. However, the configuration of the magnetic field will vary with time. In the later accretion phase, by which time a large fraction of the cloud mass has fallen onto the central region, a fan-shaped configuration would be realized. On the other hand, in the very early phase, the configuration of the magnetic field would be represented more nearly by a uniform-parallel configuration as shown in Figure 1.

To confirm the configuration of the magnetic field in the later accretion phase, Figure 15 plots magnetic field lines for the alignment model B4 ($\theta_0 = 0°$), the misalignment model B5 ($\theta_0 = 45°$) and the perpendicular model B6 ($\theta_0 = 90°$) at the end of the calculation. In B4, we can confirm an hourglass structure on the large scale and a fan-shaped configuration on the small scale. On the other hand, in B6, a nearly hourglass structure appears on the large scale, while a highly twisted configuration of magnetic field lines can be seen on the small scale. Thus, we can confirm a rough agreement between schematic view (Figure 1) and magnetic field lines derived from the simulations (Figure 15). However, more realistically, the magnetic field lines have a very complicated configuration. For example, in the alignment model B4, the poloidal components of magnetic field have a fan-shaped configuration, while strong toroidal components also exist. A strong toroidal field would thicken the pseudodisk, as pointed out by Hennebelle &
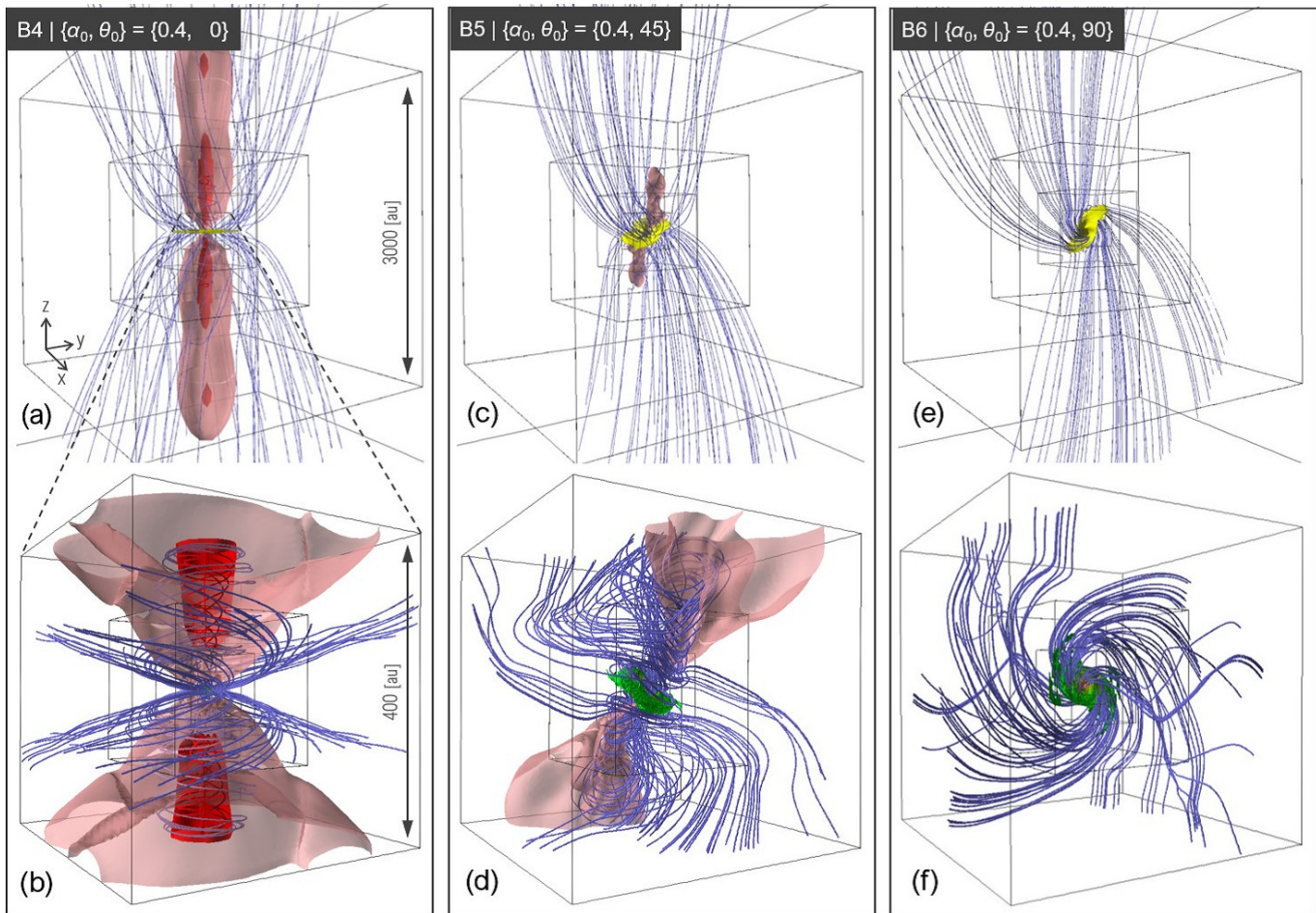
Figure 15. Three-dimensional view of magnetic field lines (blue streamlines) for models B4 ($\theta_0 = 0°$; panels a and b), B5 ($\theta_0 = 45°$; c and d), and B6 ($\theta_0 = 90°$; e and f) at $t_{\rm ps} = 5000\,{\rm yr}$. Outflow (pink and red isovelocity surfaces of $v_{\rm rad} = 1$ and $3\,{\rm km\,s^{-1}}$, respectively), pseudodisk (yellow isodensity surface of $n_{\rm H} = 5 \times 10^8\,{\rm cm^{-3}}$), and Keplerian disk (green surface) are also plotted. The box sizes are 3000 (top) and 400 au (bottom), respectively.

Ciardi (2009). In addition, a very complicated configuration of magnetic field lines is realized in B5. For this model, it is very difficult to model the configuration of the magnetic field.[7]

In the aligned case, the magnetic field configuration is changed from a uniform parallel to a fan-shaped configuration as shown in Figure 15. As described in §2, the magnetic braking is more effective in a fan-shaped configuration than in uniform parallel configuration. Thus, the change of the disk size between the alignment and misalignment models during the mass accretion phase is partly owing to the change of the magnetic field configuration. However, since the configuration of the magnetic field varies with time, it is very difficult to estimate the

moment of inertia and the efficiency of the magnetic braking from the simulations.

In addition to the change in the magnetic configuration, the outflow strength would be related to the disk formation (Li et al. 2013). Also, the existence of a flattened pseudodisk may affect the disk evolution (Hennebelle & Ciardi 2009). With these simulations, we confirm that all the factors (initial angle difference, magnetic field configuration, outflow emergence, existence of thick pseudodisk, and gravitational stability) described in past studies are relevant to determining the disk properties. We do not identify which mechanism is the most effective because it should depend on the initial conditions of the prestellar clouds such as density and velocity distributions, magnetic field strength, and rotation rate.

Finally, we comment on the non-ideal MHD effects. Hennebelle & Ciardi (2009) and Joos et al. (2012) claimed that no disk appears when the magnetic field

---

[7] The magnetic field lines for these models can be seen from various viewing angles at the following link (https://jupiter.geo.kyushu-u.ac.jp/hirano/MHDdisk.html).
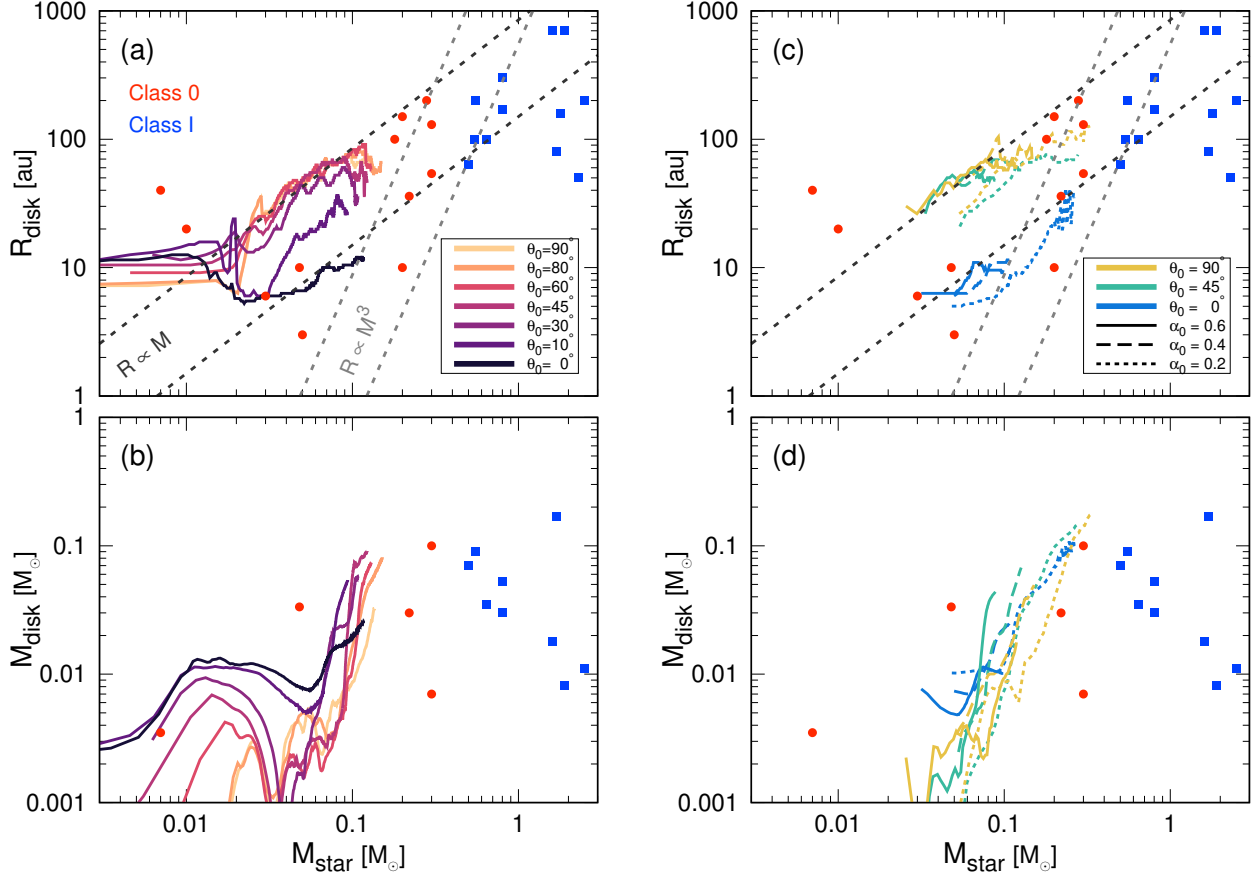
Figure 16.   Time sequence of disk radius (panels a and c) and disk mass (b and d) against the protostellar mass for all models in Simulations A (left) and B (right). The observation data of Class 0 (red circle) and Class I (blue square) protostars (Jørgensen et al. 2009; Yen et al. 2015, 2017; Okoda et al. 2018) are also plotted. Black and gray dotted lines in the top panels are models of Terebey et al. (1984) and Basu (1998).

is as strong as $\mu_0 \lesssim 5$.[8] However, with such a strong magnetic field, a Keplerian disk appears and is maintained for $\sim 5000\,\mathrm{yr}$ in our study, as in those of Masson et al. (2016) and Tsukamoto et al. (2018). The difference among the studies is in whether or not non-ideal MHD effects are included. In the alignment case, a small Keplerian disk can form when a strong magnetic field as well as non-ideal MHD effects are included.

6. COMPARISON WITH OBSERVATIONS

As shown in §4, a Keplerian disk appears in all models. However, the disk size depends on the parameter θ_0. In this section, we compare the disk size derived from simulations with that from observations, in order to verify the simulation results.

Figure 16 shows the time sequence of disk radius R_{disk} for all models against protostellar mass M_{star}, in which

the observed disk radius for Class 0, 0/I, and I protostars are superimposed. Although there are some exceptions, the disk radius taken from the simulations are comparable to the observations. For models A1–A7 (panel a), we only changed θ_0, while other parameters of the prestellar core such as mass, radius, magnetic field strength and rotation rate are fixed. Nevertheless, the disk sizes are in rough agreement with observations. Figures 16(c) and (d) indicate that the dependence of the disk size and mass on α_0 is weaker than on θ_0. The variability in disk radius can be explained only by the initial angle difference. This means that the initial angle difference may be a significant factor in determining the disk properties. Note that since the protostellar mass is $\sim 0.1 M_\odot$ at the end of our simulations, we cannot compare simulation results with observations in the range of $M_{\mathrm{star}} \gtrsim 0.1 M_\odot$. We need a further time integration of simulations to compare with observed data at later stages. In addition, we require more samples at earlier stages ($M_{\mathrm{star}} \lesssim 0.1 M_\odot$) in observations to more reliably compare observations with simulations.

---

[8] Li et al. (2013) imposed a constant artificial resistivity to some models. However, in their study, since the sink radius is too large to capture the disk (see §2), we do not comment on it here.

Finally, we comment on the oscillation in the disk radius and mass. In Figure 16(b), the disk masses have a local peak around $M_{\rm star} \sim 0.01\,M_\odot$, at which the disk mass $M_{\rm disk}$ is comparable to the protostellar mass $M_{\rm star}$. In such a situation, gravitational instability occurs and the gas in the disk rapidly falls onto the central protostar. As shown in Figure 8(a), the mass accretion rate shows a high time variability. After the rapid mass accretion, the disk mass rapidly decreases and the disk radius temporally increases due to the conservation of angular momentum (Machida et al. 2010; Tomida et al. 2017). Note that after the rapid mass accretion, the disk mass decreases while the angular momentum remains, leading to the increase of disk radius. The same phenomenon occurs at $M_{\rm star} \sim 0.1\,M_\odot$, when the disk mass again becomes comparable to the protostellar mass. Thus, the rapid increase and decrease in the disk radius seen in Figure 8 can be explained by the gravitational instability (Figure 6l). Although we do not further model the gravitational instability, which is outside the scope of this study (for details, also see Machida et al. 2014; Machida & Basu 2019; Hirano & Machida 2019), we see that the disk size can be changed in a short duration.

7. SUMMARY

In order to resolve the long-standing debate about misalignment, we investigated the star formation process in clouds with the rotation axis inclined against the global magnetic field using 3D non-ideal (resistive) MHD simulations. We obtained the following results:

- In the very early accretion phase, the disk is larger and more massive in the alignment model ($\theta_0 = 0°$) than in the misalignment models ($\theta_0 \neq 0°$), which is consistent with Matsumoto & Tomisaka (2004) and Tsukamoto et al. (2018). On the other hand, in the later accretion phase, the disk radius and mass in the alignment model are the smallest among the models, which is consistent with Hennebelle & Ciardi (2009) and Joos et al. (2012).

- The configuration of magnetic field gradually changes in the accretion phase. In the later accretion phase, the magnetic field has a fan-like configuration in the alignment model, while it has a spiral configuration in the perpendicular model ($\theta_0 = 90°$). The time variation of magnetic configuration changes the efficiency of magnetic braking, which results in the change of the disk properties.

- As time proceeds the disk radius and mass in the alignment model becomes relatively small, while those in the misalignment models becomes relatively large. In the later accretion phase, the disk radius and mass in the misalignment models are several times larger than those in the alignment model.

- The outflow is weaker in the misalignment models than in the alignment model, as seen in Li et al. (2013) and Lewis et al. (2015). A very weak outflow appears in the perpendicular case.

- In the misalignment models, the outflow direction does not agree with that of the global magnetic field because the outflow emerges in the disk normal direction, which roughly corresponds to the rotation vector of the initial cloud. The misalignment between outflow and global magnetic field seen in the simulations can provide a reasonable explanation for some observations (Hull et al. 2013).

- The gravitational stability (or the ratio of thermal to gravitational energy) of the initial cloud also affects the disk formation and outflow driving. A large-sized disk and strong outflow tend to appear in an initially unstable cloud, while a small-sized disk and a weak outflow are seen in an initial nearly stable cloud. In addition, the initial angle difference between the rotation axis and magnetic field does not significantly affect the disk evolution and outflow driving when the initial cloud is in a highly unstable state.

Our simulations showed that the misalignment promotes the disk formation and suppresses the outflow driving in the gas accretion phase. Figure 17 shows that tendency of the disk properties and outflow strength. The figure indicates that a massive and large-sized disk tends to appear in the cloud with a large θ_0 and a small α_0, while a less massive and small-sized disk appears with a small θ_0 and a large α_0.[9] is not very simple and the most massive disk appears around $\theta_0 = 45°$ at the end of the simulation ($t_{\rm ps} = 5000\,{\rm yr}$). However, the difference in the disk mass among misaligned models ($\theta_0 \neq 0°$) is very small and the disk mass shows a high time variability. Thus, the tendency is expected to be changed in further time integration. The tendency of the protostellar mass is almost the same as in the disk mass and radius: a massive protostar appears with a large θ_0 and a small α_0 and vice versa. However, it is not clear whether or not the parameter dependence shown in this study is maintained even in the later accretion phase. Further long-term calculations are necessary to make a conclusion.

In our simulation, unlike Hennebelle & Ciardi (2009) and Joos et al. (2012), a Keplerian disk appears even in the alignment case, although the disk size in the alignment case is significantly smaller than in the misalignment case. The difference between our study and Hennebelle & Ciardi (2009) and Joos et al. (2012) is the inclusion of non-ideal MHD effect. In reality, the forma-

[9] The dependence of the disk mass on θ_0
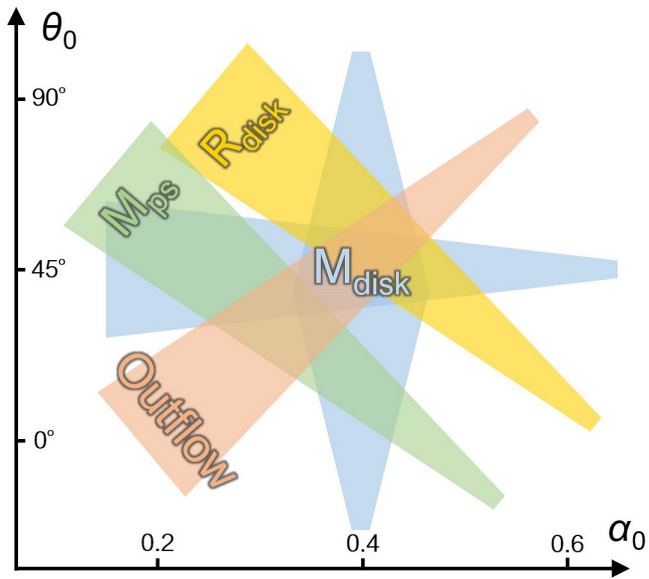
Figure 17. Schematic view of disk size (yellow), disk mass (blue), protostellar mass (green), and outflow strength (orange) in the parameter space, α_0 and θ_0. The properties are large in the wide region, while they are small in the narrow region. Each value is described in Table 1.

tion of a rotationally-supported disk in the alignment

case was confirmed in recent non-ideal MHD simulations (Masson et al. 2016; Tsukamoto et al. 2018). Also, the outflow appears even in the misalignment case, while the outflow in the perpendicular case is much weaker than in other cases. Thus, although the misalignment nature quantitatively changes the properties of disk and outflow, it does not qualitatively change the star formation process.

APPENDIX

A. NUMERICAL CONVERGENCE

We ran additional sets of simulations in order to test the numerical convergence of the results. While we used 64^3 cells in each refinement level for the models in the main text, we re-ran models A1, A4, and A7 with higher resolution grids, 128^3 cells in each refinement level. We stopped the runs at $t_{ps} = 1000\,\mathrm{yr}$ after the protostar formation because of the higher computational cost.

Figure A1 shows the density distributions at $t_{ps} = 1000\,\mathrm{yr}$. The effect of different numerical resolutions can be found by comparing the upper (128^3 cells) and lower (64^3 cells) panels. There is no significant difference in the overall structure of the rotation disk and expanding outflow. Figure A2 summarizes the analyzed disk quantities. In the aligned models (A1), the disk quantities in the higher resolution case show the similar track to the standard case. In the misaligned and perpendicular cases (A4 and A7), there are some differences in the disk quantities in the early phase ($t_{ps} < 400\,\mathrm{yr}$). However, the differences becomes small as time proceeds. Furthermore, the dependence of physical quantities on the misalignment parameter (θ_0) are qualitatively the same between the two resolution cases, as shown in each panel

of Figure A2. Thus, we conclude that the simulation results in this study are qualitatively not significantly affected by the numerical resolution.

B. SYMMETRY BREAKING IN PERPENDICULAR MODELS

The initial clouds adopted in this study have a spatial symmetry such as point symmetry to the origin for the misaligned models and both mirror symmetry to the $y = 0$ plane and point symmetry to the origin for the perpendicular models (see Figure 1). Such symmetries should be maintained during the calculation. We can confirm symmetric structures in the aligned and misaligned models in Figure 2. However, the symmetry is somewhat broken in the perpendicular models due to the numerical perturbation, which may generate a harmful effect.

To test whether or not the symmetry breaking affects the simulation results and analysed properties, we performed an additional run for perpendicular model A7, artificially imposing both the mirror symmetry to the $y = 0$ plane and point symmetry to the origin (hereafter we call this model A7sym). Figure B3(a) shows the density distribution on the $y = 0$ plane at $t_{ps} = 5000\,\mathrm{yr}$
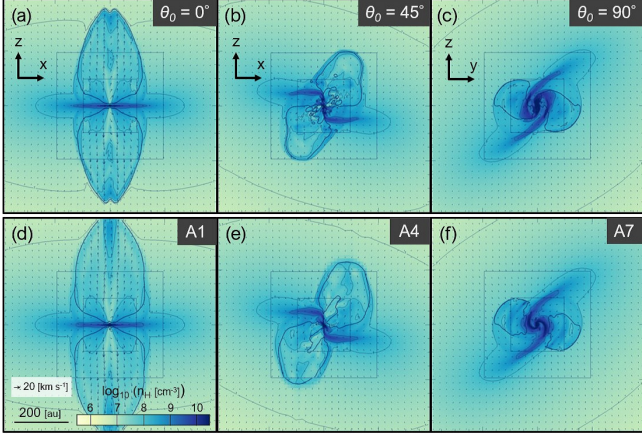
Figure A1. Same as in Figure 2, but for models A1, A4, and A7 with higher resolution grids, with 128^3 cells in each refinement level (top panels), and with standard grids, with 64^3 cells (bottom panels), respectively, at $t_{ps} = 1000\,\mathrm{yr}$ after protostar formation. The two panels on the left and the right panel show the $y = 0$ and $x = 0$ planes, respectively.

after protostar formation for models A7sym (top panels) and A7 (bottom panels). The overall structure of model A7sym is very similar to the original run (model A7), in which we did not impose any artificial symmetry in model A7 (Figure B3c). Especially, the rotation disks are almost the same regardless of whether or not symmetry breaking occurs (Figures B3b and d). Figure B4 shows that the disk properties are almost the same between the two runs.
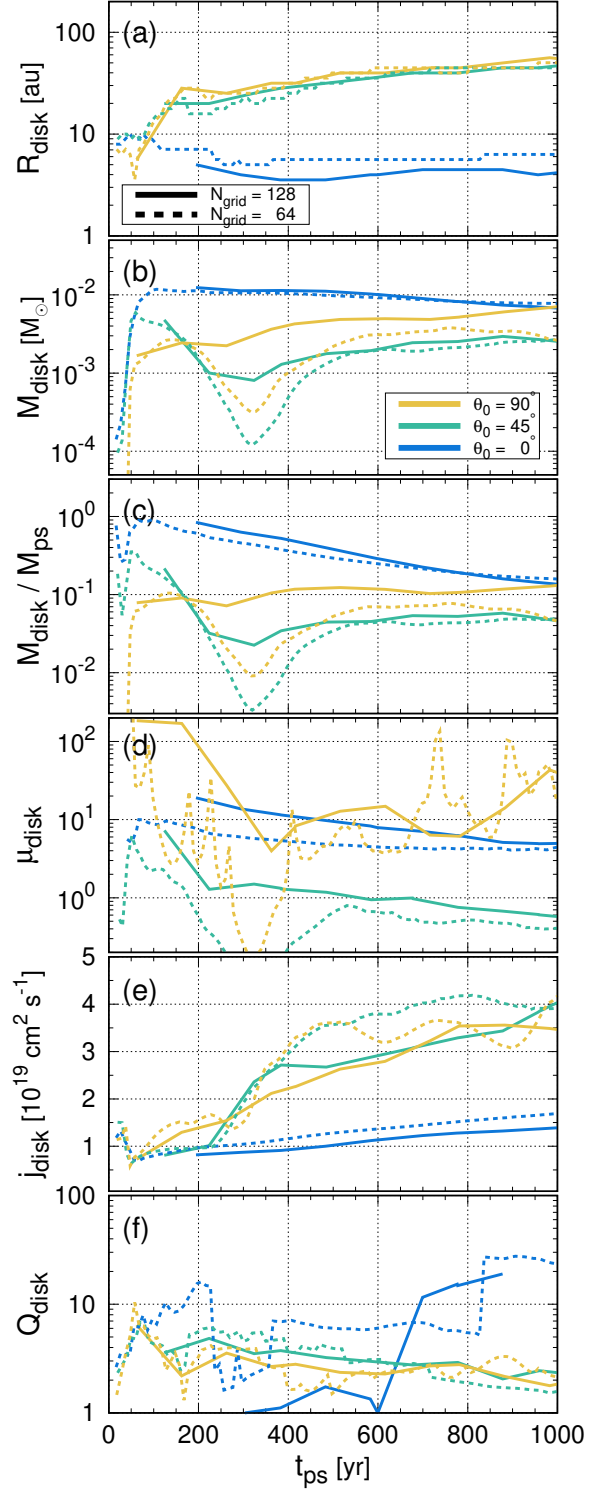

Figure A2. Same as in Figure 6, but with higher resolution grid models A1, A4, and A7. The higher resolution grid models (128^3 cells in each refinement level) are plotted by solid lines, while the standard grids models (64^3 cells) are by the dashed line. The calculations were executed until $t_{ps} = 1000\,\mathrm{yr}$ after protostar formation
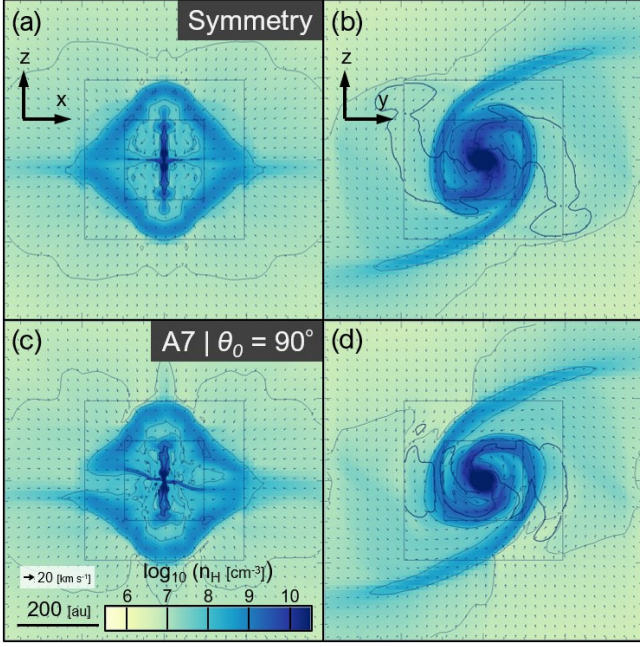
Figure B3. Same as in Figure 2, but only for models A7 and A7sym ($\theta_0 = 90°$). The mirror and point symmetries are artificially imposed in the top panels (panels a and b), while no artificial symmetry is imposed in the bottom panels (panels c and d). The calculation results at $t_{\rm ps} = 5000\,{\rm yr}$ after protostar formation are plotted on the $y = 0$ (left panels) and $x = 0$ (right panels) planes.
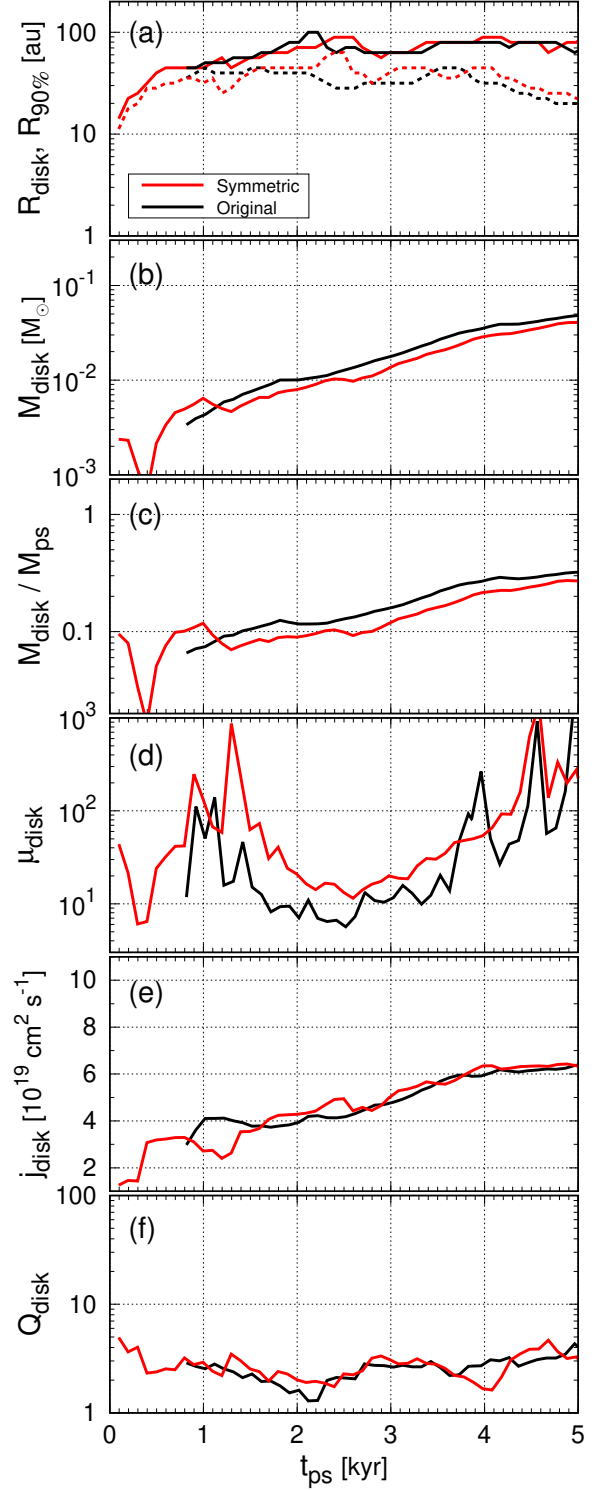

Figure B4. Same as in Figure 6. The calculation results for models A7sym (red) and A7 (black, A7). Each quantity is plotted against the elapsed time after protostar formation.

REFERENCES

Andrews, S. M., Huang, J., Pérez, L. M., et al. 2018, ApJL, 869, L41

Aso, Y., Ohashi, N., Saigo, K., et al. 2015, ApJ, 812, 27

Aso, Y., Ohashi, N., Aikawa, Y., et al. 2017, ApJL, 850, L2

Allen, A., Li, Z.-Y., & Shu, F. H. 2003, ApJ, 599, 363

Alves, F. O., Girart, J. M., Caselli, P., et al. 2017, A&A, 603, L3

Banerjee, R., & Pudritz, R. E. 2006, ApJ, 641, 949

Basu, S., & Mouschovias, T. C. 1994, ApJ, 432, 720

Basu, S., & Mouschovias, T. C. 1995a, ApJ, 452, 386

Basu, S., & Mouschovias, T. C. 1995b, ApJ, 453, 271

Basu, S. 1998, ApJ, 509, 229

Bjerkeli, P., van der Wiel, M. H. D., Harsono, D., Ramsey, J. P., & Jørgensen, J. K. 2016, Nature, 540, 406

Ching, T.-C., Lai, S.-P., Zhang, Q., et al. 2016, ApJ, 819, 159

Ciardi, A., & Hennebelle, P. 2010, MNRAS, 409, L39

Dapp, W. B., & Basu, S. 2010, A&A, 521, L56

Dapp, W. B., Basu, S., & Kunz, M. W. 2012, A&A, 541, A35

Gray, W. J., McKee, C. F., & Klein, R. I. 2018, MNRAS, 473, 2124

Hara, C., Shimajiri, Y., Tsukagoshi, T., et al. 2013, ApJ, 771, 128

Hsieh, T.-H., Murillo, N. M., Belloche, A., et al. 2018, ApJ, 854, 15

Hennebelle, P., & Ciardi, A. 2009, A&A, 506, L29

Hennebelle, P., Commerçon, B., Chabrier, G., et al. 2016, ApJL, 830, L8

Hirano, S., & Machida, M. N. 2019, MNRAS, 485, 4667

Hirota, T., Machida, M. N., Matsushita, Y., et al. 2017, Nature Astronomy, 1, 0146

Hull, C. L. H., Plambeck, R. L., Bolatto, A. D., et al. 2013, ApJ, 768, 159

Inutsuka, S.-i. 2012, Progress of Theoretical and Experimental Physics, 2012, 01A307

Joos, M., Hennebelle, P., & Ciardi, A. 2012, A&A, 543, A128

Joos, M., Hennebelle, P., Ciardi, A., & Fromang, S. 2013, A&A, 554, A117

Jørgensen, J. K., van Dishoeck, E. F., Visser, R., et al. 2009, A&A, 507, 861

Koga, S., Tsukamoto, Y., Okuzumi, S., & Machida, M. N. 2019, MNRAS, 484, 2119

Krasnopolsky, R., Li, Z.-Y., & Shang, H. 2011, ApJ, 733, 54

Krumholz, M. R., Crutcher, R. M., & Hull, C. L. H. 2013, ApJL, 767, L11

Lefloch, B., Gusdorf, A., Codella, C., et al. 2015, A&A, 581, A4

Lee, C.-F., Ho, P. T. P., Li, Z.-Y., et al. 2017, Nature Astronomy, 1, 0152

Lee, C.-F., Li, Z.-Y., Hirano, N., et al. 2018, ApJ, 863, 94

Lewis, B. T., Bate, M. R., & Price, D. J. 2015, MNRAS, 451, 288

Li, Z.-Y., & McKee, C. F. 1996, ApJ, 464, 373

Li, Z.-Y., Krasnopolsky, R., & Shang, H. 2013, ApJ, 774, 82

Li, Z.-Y., Banerjee, R., Pudritz, R. E., et al. 2014, Protostars and Planets VI, 173

Machida, M. N., & Basu, S. 2019, ApJ, 876, 149

Machida, M. N., Tomisaka, K., & Matsumoto, T. 2004, MNRAS, 348, L1

Machida, M. N., Matsumoto, T., Tomisaka, K., & Hanawa, T. 2005, MNRAS, 362, 369

Machida, M. N., Matsumoto, T., Hanawa, T., & Tomisaka, K. 2006, ApJ, 645, 1227

Machida, M. N., Inutsuka, S.-i., & Matsumoto, T. 2007, ApJ, 670, 1198

Machida, M. N., Inutsuka, S.-i., & Matsumoto, T. 2010, ApJ, 724, 1006

Machida, M. N., Inutsuka, S.-I., & Matsumoto, T. 2011, PASJ, 63, 555

Machida, M. N., & Matsumoto, T. 2012, MNRAS, 421, 588

Machida, M. N., & Hosokawa, T. 2013, MNRAS, 431, 1719

Machida, M. N., Inutsuka, S.-i., & Matsumoto, T. 2014, MNRAS, 438, 2278

Machida, M. N., Matsumoto, T., & Inutsuka, S.-i. 2016, MNRAS, 463, 4246

Machida, M. N., Hirano, S., & Kitta, H. 2020, MNRAS, 491, 2180

Marchand, P., Masson, J., Chabrier, G., et al. 2016, A&A, 592, A18

Masson, J., Chabrier, G., Hennebelle, P., Vaytet, N., & Commerçon, B. 2016, A&A, 587, A32

Matsumoto, T., & Tomisaka, K. 2004, ApJ, 616, 266

Matsumoto, T., Nakazato, T., & Tomisaka, K. 2006, ApJL, 637, L105

Matsumoto, T., Machida, M. N., & Inutsuka, S.-i. 2017, ApJ, 839, 69

Matsushita, Y., Machida, M. N., Sakurai, Y., & Hosokawa, T. 2017, MNRAS, 470, 1026

Matsushita, Y., Sakurai, Y., Hosokawa, T., & Machida, M. N. 2018, MNRAS, 475, 391

Mellon, R. R., & Li, Z.-Y. 2008, ApJ, 681, 1356

Mellon, R. R., & Li, Z.-Y. 2009, ApJ, 698, 922

Mouschovias, T. C., & Spitzer, L. Jr. 1976, ApJ, 210, 2326

Mouschovias, T. C., & Paleologou, E. V. 1979, ApJ, 230, 204

Mouschovias, T. C., & Paleologou, E. V. 1980a, Moon and Planets, 22, 31

Mouschovias, T. C., & Paleologou, E. V. 1980b, ApJ, 237, 877

Mouschovias, T. C. 1983, Solar and Stellar Magnetic Fields: Origins and Coronal Effects, 102, 479

Mouschovias, T. C., & Morton, S. A. 1985, ApJ, 298, 190

Mouschovias, T. C. 1985, A&A, 142, 41

Mouschovias, T. C., & Paleologou, E. V. 1986, ApJ, 308, 781

Ohashi, N., Saigo, K., Aso, Y., et al. 2014, ApJ, 796, 131

Okoda, Y., Oya, Y., Sakai, N., et al. 2018, ApJL, 864, L25

Pérez, L. M., Carpenter, J. M., Andrews, S. M., et al. 2016, Science, 353, 1519

Plunkett, A. L., Arce, H. G., Mardones, D., et al. 2015, Nature, 527, 70

Sakai, N., Sakai, T., Hirota, T., et al. 2014, Nature, 507, 78

Santos-Lima, R., de Gouveia Dal Pino, E. M., & Lazarian, A. 2013, MNRAS, 429, 3371

Seifried, D., Banerjee, R., Pudritz, R. E., et al. 2012, MNRAS, 423, L40

Seifried, D., Banerjee, R., Pudritz, R. E., et al. 2013, MNRAS, 432, 3320

Tassis, K., & Mouschovias, T. C. 2005, ApJ, 618, 783

Terebey, S., Shu, F. H., & Cassen, P. 1984, ApJ, 286, 529

Truelove, J. K., Klein, R. I., McKee, C. F., et al. 1998, ApJ, 495, 821

Tobin, J. J., Hartmann, L., Chiang, H.-F., et al. 2012, Nature, 492, 83

Tomida, K., Tomisaka, K., Matsumoto, T., et al. 2013, ApJ, 763, 6

Tomida, K., Okuzumi, S., & Machida, M. N. 2015, ApJ, 801, 117

Tomida, K., Machida, M. N., Hosokawa, T., Sakurai, Y., & Lin, C. H. 2017, ApJL, 835, L11

Tomisaka, K. 2002, ApJ, 575, 306

Toomre, A. 1964, ApJ, 139, 1217

Tsukamoto, Y., Iwasaki, K., Okuzumi, S., Machida, M. N., & Inutsuka, S. 2015, MNRAS, 452, 278

Tsukamoto, Y., Iwasaki, K., Okuzumi, S., Machida, M. N., & Inutsuka, S. 2015b, ApJ, 810, 26

Tokuda, K., Onishi, T., Matsumoto, T., et al. 2016, ApJ, 826, 26

Tsukamoto, Y. 2016, PASA, 33, e010

Tsukamoto, Y., Okuzumi, S., Iwasaki, K., Machida, M. N., & Inutsuka, S. 2017, PASJ, 69, 95

Tsukamoto, Y., Okuzumi, S., Iwasaki, K., Machida, M. N., & Inutsuka, S. 2018, ApJ, 868, 22

Wurster, J., & Li, Z.-Y. 2018a, Frontiers in Astronomy and Space Sciences, 5, 39

Wurster, J., Bate, M. R., & Price, D. J. 2018b, MNRAS, 476, 2063

Yen, H.-W., Koch, P. M., Takakuwa, S., et al. 2015, ApJ, 799, 193

Yen, H.-W., Koch, P. M., Takakuwa, S., et al. 2017, ApJ, 834, 178

Zhao, B., Caselli, P., Li, Z.-Y., et al. 2016, MNRAS, 460, 2050

Zhao, B., Caselli, P., & Li, Z.-Y. 2018, MNRAS, 478, 2723